energy&fuels

pubs.acs.org/EF Article

Simulation Study on the All-Inorganic $CsSn_xGe_{1-x}I_3$-Based Perovskite Solar Cells Using Isotypic Perovskites as Hole Transport Layers

Shuo Lin, Baoping Zhang, Weichao Wang, Tie-Yu Lü, Jinrong Zhou, Xiuyan Li, Yuhong Fang, and Jin-Cheng Zheng*

Cite This: *Energy Fuels* 2024, 38, 19831−19846

Read Online

ACCESS | Metrics & More | Article Recommendations | SI Supporting Information

Downloaded via XIAMEN UNIV on October 17, 2024 at 08:35:25 (UTC).
See https://pubs.acs.org/sharingguidelines for options on how to legitimately share published articles.

ABSTRACT: All-inorganic Sn−Ge-based perovskite solar cells (PSCs) have made great progress in recent years. Furthermore, they can be used as promising lead-free absorbers for PSCs, and *p*-type-doped $CsSnI_3$, $CsGeI_3$, and $CsSn_{0.5}Ge_{0.5}I_3$ could also be used as good hole transport layers (HTLs). In this simulation work, $CsSnI_3$, $CsGeI_3$, and $CsSn_{0.5}Ge_{0.5}I_3$ are used as both absorbers and HTLs. The effects of the dopant concentration of HTLs, the thickness of absorbers, and HTLs on the photovoltaic performance of PSCs were studied to optimize the device structures. The maximum efficiencies from high to low are 28.35%, 26.35%, 25.84%, 25.23%, 18.83%, 17.49%, and 11.79% for the TiO_2/*i*-$CsSnI_3$/*p*-$CsSnI_3$, TiO_2/*i*-$CsSn_{0.5}Ge_{0.5}I_3$/*p*-$CsSn_{0.5}Ge_{0.5}I_3$, TiO_2/*i*-$CsSn_{0.5}Ge_{0.5}I_3$/*p*-$CsSnI_3$, TiO_2/*i*-$CsSnI_3$/*p*-$CsGeI_3$, TiO_2/*i*-$CsSn_{0.5}Ge_{0.5}I_3$/*p*-$CsGeI_3$, TiO_2/*i*-$CsGeI_3$/*p*-$CsGeI_3$, and TiO_2/*i*-$CsGeI_3$/*p*-$CsSnI_3$, respectively. The TiO_2/*i*-$CsGeI_3$/*p*-$CsSnI_3$ cell exhibits the lowest efficiency of 11.79% in all of the simulated PSCs due to the spike-like band offset at the *i*-$CsGeI_3$/*p*-$CsSnI_3$ interface and high recombination rate in the *p*-$CsSnI_3$ region. It is found that the *n*-*p* structures could have better photovoltaic performance (thickness of *i*-film approaching zero) than the conventional *n*-*i*-*p* structures for the TiO_2/*i*-$CsSnI_3$/*p*-$CsSnI_3$, TiO_2/*i*-$CsGeI_3$/*p*-$CsGeI_3$, and TiO_2/*i*-$CsSn_{0.5}Ge_{0.5}I_3$/*p*-$CsSn_{0.5}Ge_{0.5}I_3$ PSCs if the defects in HTLs created by high doping can be effectively controlled. The efficiencies of PSCs are sensitive to the defect density and defect level position, and the influence of defect density on the PV performance is larger than that of the defect level position. The solar cells could maintain high power conversion efficiency for defect density below about 5×10^{17} cm^{-3}. Furthermore, the increase of the interface trap density is found to reduce the photovoltaic performance of PSCs. Our study provides insight into the optimal design of $CsSn_xGe_{1-x}I_3$-based PSCs.

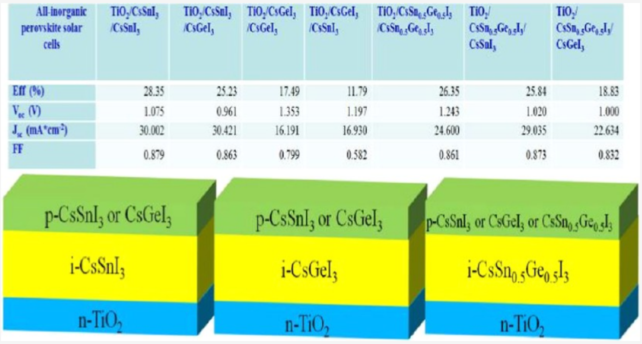

All-inorganic perovskite solar cells	$TiO_2/CsSnI_3$ $/CsSnI_3$	$TiO_2/CsSnI_3$ $/CsGeI_3$	$TiO_2/CsGeI_3$ $/CsGeI_3$	$TiO_2/CsGeI_3$ $/CsSnI_3$	$TiO_2/CsSn_{0.5}Ge_{0.5}I_3$ $/CsSn_{0.5}Ge_{0.5}I_3$	$TiO_2/$ $CsSn_{0.5}Ge_{0.5}I_3/$ $CsSnI_3$	$TiO_2/$ $CsSn_{0.5}Ge_{0.5}I_3/$ $CsGeI_3$
Eff (%)	28.35	25.23	17.49	11.79	26.35	25.84	18.83
V_{oc} (V)	1.075	0.961	1.353	1.197	1.243	1.020	1.000
J_{sc} ($mA*cm^{-2}$)	30.002	30.421	16.191	16.930	24.600	29.035	22.634
FF	0.879	0.863	0.799	0.582	0.861	0.873	0.832

1. INTRODUCTION

Due to their excellent photoelectric properties, perovskite solar cells (PSCs) have emerged as a breakthrough photovoltaic (PV) technology, holding unprecedented promise for high-efficiency, low-cost solar cells. While the record power conversion efficiency (PCE) of PSCs has exceeded 26%,[1−5] rivaling that of silicon-based solar cells, the state-of-the-art PSCs employ lead-based organic−inorganic halide perovskite absorber materials. However, the toxicity and instability caused by the lead and organic components are the main challenges on the way to realizing large-scale commercialization. Incorporating Cs in the perovskite precursor is shown to be promising for enhancing the stability and performance of methylammonium (MA)-free PSCs.[6] Unlike the mobile nature of MA and Br and their volatility that make the final amount of MA or Br in the perovskite unknown, Cs incorporation as a nonvolatile ionic species in the perovskite solution remains in the final film.[6] Considering a low-toxicity or nontoxic inorganic perovskite, Sn(II) and Ge(II) were used to replace Pb cations. $CsSnI_3$ (E_g = 1.3 eV), $CsGeI_3$ (E_g = 1.63 eV), and $CsSn_xGe_{1-x}I_3$ perovskites have been studied comprehensively and shown to possess favorable photoelectric properties for PV application, such as suitable direct band gaps for solar spectrum ($CsSnI_3$ and $CsGeI_3$),[7,8] high charge-carrier mobility,[7,9,10] high stability,[7,10] low exciton binding energy,[7,11,12] etc. In recent years, there have been two significant breakthroughs in these fields.[10,13−15] First, most of the reported PCEs for $CsSnI_3$-based PSCs were only between 3 and 5% before 2021,[13] but in 2021, Li et al.[13] reported a PCE of 8.2% for $CsSnI_3$ PSCs, and Ye et al.[14] reported PCEs of 10.1 and 9.6%. Their (Ye et al.) encapsulated devices maintain 94.3%, 83.4%, and 81.3% of the efficiencies under inert (60 days), ambient (45 days), and 1 Sun continuous illumination under ∼70 °C

Received: August 16, 2024
Revised: September 21, 2024
Accepted: September 24, 2024
Published: October 7, 2024

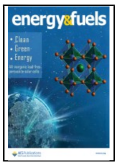

ACS Publications

© 2024 American Chemical Society

https://doi.org/10.1021/acs.energyfuels.4c03960

(2000 min) conditions, respectively.[14] Very recently, Duan et al.[15] reported 11.2% (May 2023) for $CsSnI_3$ PSCs, which is the highest efficiency of $CsSnI_3$ PSCs reported to date. Second, in 2019, Chen et al.[10] demonstrated the use of the lead-free, all-inorganic $CsSn_{0.5}Ge_{0.5}I_3$ perovskite as the light absorber in PSCs, delivering promising efficiency of up to 7.11%. More importantly, these PSCs show very high stability, with less than 10% decay in efficiency after 500 h of continuous operation in a N_2 atmosphere under one-sun illumination.[10] The efficiency progress of $CsSnI_3$, $CsGeI_3$, and $CsSn_{0.5}Ge_{0.5}I_3$ PSCs is shown in Figure 1. The aforementioned considerations provide the rationale for the study of $CsSnI_3$, $CsGeI_3$, and $CsSn_{0.5}Ge_{0.5}I_3$ as promising inorganic, lead-free, thermally stable perovskites for next-generation PSCs.

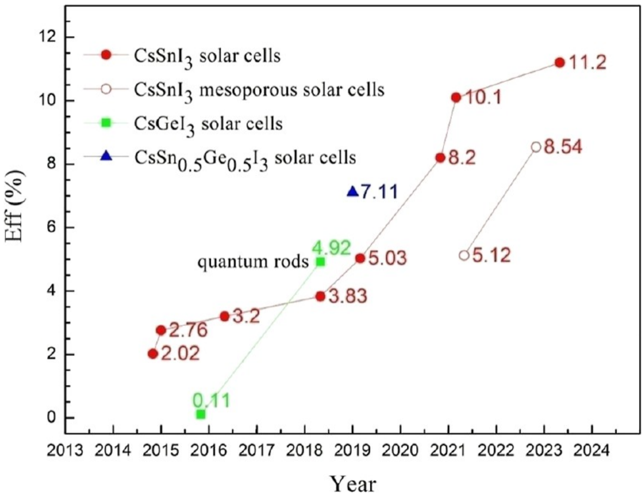

Figure 1. Efficiency progress of all-inorganic $CsSn_xGe_{1-x}I_3$-based PSCs including $CsSnI_3$, $CsGeI_3$, and $CsSn_{0.5}Ge_{0.5}I_3$ PSCs over recent years.[10,13−19]

On the one hand, $CsSnI_3$, $CsGeI_3$, and $CsSn_{0.5}Ge_{0.5}I_3$ are promising perovskite absorber materials, and on the other hand, with high *p*-type doping, they could also be used as good hole transport layers (HTLs) for PSCs,[20,21] which are also very important in high-efficiency PSCs. First, $CsSnI_3$, $CsGeI_3$, and $CsSn_{0.5}Ge_{0.5}I_3$ have high charge-carrier mobility.[7,9,10] Second, they can be doped as *p*-type semiconductors for hole transports (the unintentionally doped $CsSnI_3$, $CsGeI_3$, and $CsSn_{0.5}Ge_{0.5}I_3$ are *p*-type semiconductors, see Table S1). The usage of isotypic perovskites as HTLs in all-inorganic Sn−Ge-based PSCs could have some advantages: good band matching and lattice matching between the absorbers and HTLs; the growth of absorbers and HTLs in the same growth equipment could be convenient, etc. Moreover, it has recently been shown that the thermoelectric transport is strongly related to asymmetry of electronic states.[22] It would be interesting to see how the electronic asymmetry of HTLs and absorbers affects the performance of PV devices. However, to the best of our knowledge, very few reports on all-inorganic $CsSn_xGe_{1-x}I_3$-based PSCs employing $CsSnI_3$, $CsGeI_3$, or $CsSn_{0.5}Ge_{0.5}I_3$ as HTLs have been found so far. Jiang and Tang[23] simulated TiO_2/$CsSnI_3$ (Sn-rich)/$CsSnI_3$ solar cells, but in their work, they mainly optimized the thickness and doping concentration of $CsSnI_3$ (Sn-rich) absorbers and did not optimize the $CsSnI_3$ HTLs.

In this simulation work, $CsSnI_3$, $CsGeI_3$, and $CsSn_{0.5}Ge_{0.5}I_3$ are used as all-inorganic lead-free absorbers for PSCs, and with *p*-type doping, they are also adopted as HTLs. A comparative study on these hole-transporting materials has been made to select the appropriate hole-transporting materials. Effects of the dopant concentration of HTLs and the thickness of absorbers and HTLs on the photovoltaic performance of PSCs are investigated to optimize the device structures and provide the theoretical possibilities of design for the PSCs. In order to seek the relation between cell performance and thickness of absorber and HTL further, analytical functions for efficiencies in terms of thickness of absorber and HTL are fitted and listed. On the comparison of the photovoltaic performance of the optimal PSCs with those HTLs, the possible reasons (band structures, material, and device parameters) behind the discrepancies of performance are investigated and discussed in detail to provide guidance for designing all-inorganic $CsSn_xGe_{1-x}I_3$-based PSCs. In addition, since hole-transporting materials with high *p*-type doping usually contain many defects, the effects of concentrations and energy level positions of defects in HTLs on the photovoltaic performance of PSCs are also studied.

2. DEVICE STRUCTURES AND MODELING FRAMEWORKS

The excitons in typical organic absorbers are Frenkel-type; therefore, the exciton binding energy has to be taken into account for the carrier separation for accurate PV device modeling, which is rather complicated.[24] In contrast, the excitons in the $CsSnI_3$, $CsGeI_3$, and $CsSn_{0.5}Ge_{0.5}I_3$ perovskites are typical Wannier-type,[7,11,12] so the photoexcited carriers can be dealt with the same manner with inorganic materials. The two facts, i.e., structural similarity without the mesoporous structure and the exciton type, enable us to apply an existing device simulator widely used in inorganic solar cells to the PSCs.[24]

In this study, AMPS-1D software[25] is used to simulate $CsSnI_3$ PSCs. AMPS-1D is a one-dimensional device physics code and based on the basic equations of semiconductors and solar cells.[25] We have successfully applied this code in the simulation of $CsSnI_3$ PSCs with diverse electron transport layers (ETLs).[7] Here, we briefly describe the main equations used in the simulation as follows:

Poisson's equation:

$$\frac{\mathrm{d}}{\mathrm{d}x}\left[\varepsilon(x)\frac{\mathrm{d}\Psi(x)}{\mathrm{d}x}\right] = q^2 \times [p(x) - n(x) + N_\mathrm{D}^{+}(x) - N_\mathrm{A}^{-}(x) + p_\mathrm{t}(x) - n_\mathrm{t}(x)] \qquad (1)$$

where the local vacuum level $\Psi(x)$ (in unit of eV), absolute dielectric constant $\varepsilon(x)$ and the free electron n, free hole p, trapped electron n_t, and trapped hole p_t, as well as the ionized donor-like doping $N_D{}^+$ and ionized acceptor-like doping $N_A{}^-$ concentrations are all functions of the position coordinate x. q is the electron charge.

Continuity equation for electrons:

$$\frac{1}{q}\left[\frac{\mathrm{d}J_\mathrm{n}(x)}{\mathrm{d}x}\right] = -G_\mathrm{L}(x) + R(x) \qquad (2)$$

Continuity equation for holes:

$$\frac{1}{q}\left[\frac{dJ_{p}(x)}{dx}\right] = G_{L}(x) - R(x) \tag{3}$$

$J_{n}(x) = n\mu_{n}\frac{dE_{f}^{n}(x)}{dx}$ and $J_{p}(x) = p\mu_{p}\frac{dE_{f}^{p}(x)}{dx}$ are the electron and hole current densities, respectively. μ_{n} and μ_{p} are the mobilities of electron and hole, respectively. E_{f}^{n} and E_{f}^{p} are the electron and hole quasi-Fermi levels, respectively. $R(x)$ is the net recombination rate resulting from direct (band-to-band) recombination and indirect (Shockley-Read-Hall) recombination traffic through the gap states. $G_{L}(x)$ is the optical generation rate.

Determining transport characteristics then becomes a task of solving the three coupled nonlinear differential eqs 1−3, each of which has two associated boundary conditions. In AMPS, these three coupled equations are solved simultaneously to obtain a set of three unknown state variables at each point in the device: the local vacuum level and the electron and hole quasi-Fermi levels. From these three state variables, the free carrier concentrations ($n(x) = \frac{2}{\sqrt{\pi}}N_{c}F_{1/2}\left[-\frac{E_{c}(x) - E_{F}^{n}(x)}{kT}\right]$ and $p(x) = \frac{2}{\sqrt{\pi}}N_{v}F_{1/2}\left[-\frac{E_{F}^{p}(x) - E_{v}(x)}{kT}\right]$, where N_{c} and N_{v} are the effective density of states (DOS) in the conduction band and the valence band, respectively. k is the Boltzmann constant, T is the temperature, and $F_{1/2}(\xi)$ is the Fermionic integral), fields ($E(x) = \frac{1}{q}\frac{d\Psi(x)}{dx}$), currents, etc., can then be computed.

The structures of simulated planar $CsSnI_3$, $CsGeI_3$, and $CsSn_{0.5}Ge_{0.5}I_3$ PSCs are shown in Figure 2. The material parameters of $CsSnI_3$, $CsGeI_3$, and $CsSn_{0.5}Ge_{0.5}I_3$ and ETLs and HTLs used in the simulations are shown in Table S1, and the band alignment of perovskites and all contact materials adopted in this study is shown in Figures 3 and S1. The electron affinity of $CsSn_{0.5}Ge_{0.5}I_3$ is larger than that of $CsSnI_3$ and $CsGeI_3$. It may be attributed to the fact that the crystal structure (symmetry) of $CsSnI_3$ (space group: *Pnma*; orthorhombic[10]) is different from those of $CsGeI_3$ and $CsSn_{0.5}Ge_{0.5}I_3$ (space group: *R*3*m*[10]). The electron affinity also depends on the electronegativity of elements,[26] alloy effects (e.g., $CsSn_{0.5}Ge_{0.5}I_3$), and surface termination (crystal plane, surface chemistry, etc.). $CsSn_{0.5}Ge_{0.5}I_3$ is a new semiconductor alloy, which has been shown to be promising PV materials.[10] Therefore, we adopted the material parameters from ref 10 for our simulation in this work. The simulation procedures similar to this work for the $CsSn_{x}Ge_{1-x}I_3$ PSCs could be performed in the case of new data being available in the future. The optimal thickness and doping concentration of TiO_2 ETLs are 30 nm and 1×10^{21} cm^{-3}, respectively, according to our previous study.[7] The lifetime model is adopted in this work, except that the DOS model is used in the simulation of defects in the HTLs. The simulation is performed under AM1.5G illumination (100 $mW{*}cm^{-2}$, 0.32−1.32 μm). The simulated *J*−*V* characteristics of FTO/PCBM (20 nm)/$CsSn_{0.5}Ge_{0.5}I_3$ (200 nm)/Spiro-OMeTAD cell are shown in Figure S3, which is verified by fitting it to the experimental data reported by Chen et al.[10] It could be shown in Figure S3 that there is a good agreement between the *J*−*V* characteristics of the simulated PSC and experimental results.

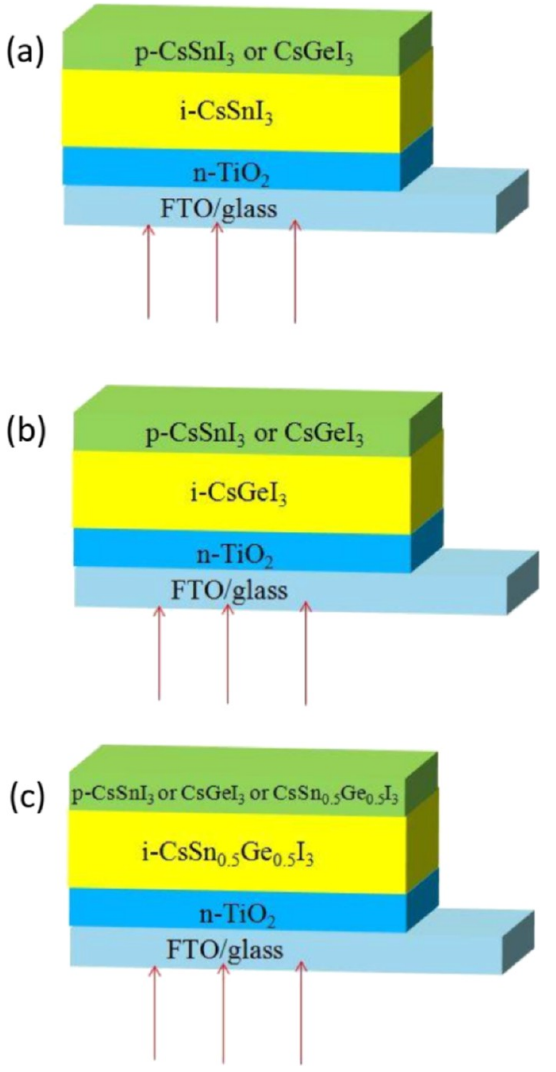

Figure 2. Structures of the simulated $CsSnI_3$, $CsGeI_3$, and $CsSn_{0.5}Ge_{0.5}I_3$ PSCs.

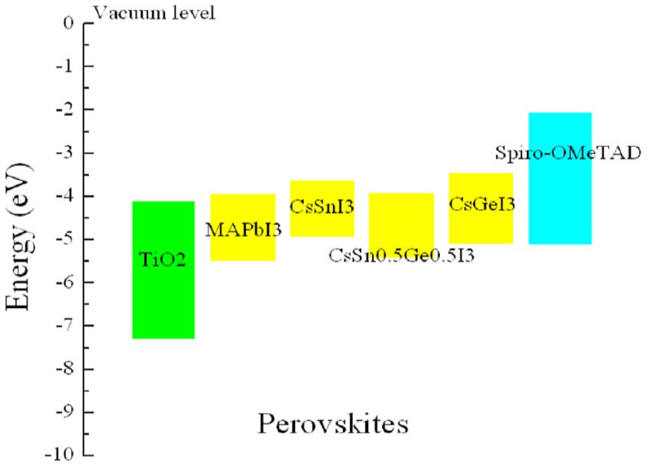

Figure 3. Energy band alignment of all-inorganic Sn−Ge-based perovskite and contact materials adopted in this study.

3. RESULTS AND DISCUSSION

3.1. Effect of the Dopant Concentrations of HTLs. In this section, the dopant concentrations of the HTLs in $CsSnI_3$,

$CsGeI_3$, and $CsSn_{0.5}Ge_{0.5}I_3$ PSCs are optimized. The initial thicknesses of absorbers and HTLs are 150 and 100 nm, respectively. Band offsets[27−30] at the heterojunctions are very important in device design and performance analyses. The conduction band offset (CBO) and valence band offset (VBO) at the perovskite/HTL interfaces are given by formulas 4 and 5, respectively, and listed in Table 1.

$$\Delta E_c = \chi(\text{HTL}) - \chi(\text{absorber}) \tag{4}$$

$$\Delta E_V = \chi(\text{HTL}) - \chi(\text{absorber}) + E_g(\text{HTL}) - E_g(\text{absorber}) \tag{5}$$

Table 1. CBO and Valence Offset at the Perovskite/HTL Interfaces

absorber	i-$CsSnI_3$	i-$CsGeI_3$	i-$Cs_{0.5}Ge_{0.5}I_3$
HTL, CBO (in unit of eV)			
p-$CsSnI_3$	0	0.17	−0.28
p-$CsGeI_3$	−0.17	0	−0.45
p-$Cs_{0.5}Ge_{0.5}I_3$			0
HTL, VBO (in unit of eV)			
p-$CsSnI_3$	0	−0.16	−0.48
p-$CsGeI_3$	0.16	0	−0.32
p-$Cs_{0.5}Ge_{0.5}I_3$			0

The positive CBO and VBO can form spike-like band offset at the perovskite/HTL interfaces, which block the drift of photogenerated carriers and lead to the degraded collection efficiency. At the i-$CsSnI_3$/p-$CsSnI_3$, i-$CsGeI_3$/p-$CsGeI_3$, and i-$Cs_{0.5}Ge_{0.5}I_3$/p-$Cs_{0.5}Ge_{0.5}I_3$ interfaces, the CBO and VBO are all zero to have good band matching, and the lattice matching is ideal.

Figure 4 shows the PV cell parameters as functions of the acceptor concentrations (N_A) of HTLs. From the figure, for all of the cells (except the TiO_2/i-$CsSn_{0.5}Ge_{0.5}I_3$/p-$CsGeI_3$ cell), the efficiencies and open-circuit voltages (V_{oc}) increase with increasing acceptor concentrations. Especially for TiO_2/i-$CsSnI_3$/p-$CsSnI_3$ (Figure 4a), TiO_2/i-$CsGeI_3$/p-$CsGeI_3$ (Figure 4c), and TiO_2/i-$CsSn_{0.5}Ge_{0.5}I_3$/p-$CsSnI_3$ (Figure 4f) cells, when the acceptor concentrations increase, the efficiencies increase rapidly. Increase in HTL dopant concentration raises the built-in electric field and electric potential at the perovskite/HTL interfaces, which enhances photogenerated carrier separation, thereby increasing the V_{oc}, fill factor (FF), and efficiencies. The short-circuit current (J_{sc}) could be improved (slightly) with increasing dopant concentrations due to the increase in the conductivity of HTLs and reduced recombination rate at the perovskite/HTL interfaces. It is noticed that the TiO_2/i-$CsGeI_3$/p-$CsSnI_3$ cell (Figure 4d) exhibits the lowest efficiencies (<10%) in all of the simulated PSCs. For the TiO_2/i-$CsGeI_3$/p-$CsSnI_3$ cell, at the i-$CsGeI_3$/p-$CsSnI_3$ interface, the positive CBO can form a spike-like band offset to block the drift of electrons, and the built-in electric field is low. Therefore, the recombination rate in the p-$CsSnI_3$ region is very high ($>10^{21}$ s^{-1} cm^{-3}), and the J_{sc} and efficiencies are low. In some cases, the PV parameters (efficiency, V_{oc}, J_{sc}, and FF) could decrease slightly with increasing HTL dopant concentrations. The decrease of PV parameters may be attributed to the change of band structures caused by the increased dopant concentrations and has been observed in the experiment for the inverted $MAPbI_3$ PSCs.[31] It is noted that, higher doping can create deep coulomb traps, which could have significant recombination effects on the photogenerated carriers and decreases charge carrier mobility.[32] However, it is not considered in this section and will be studied and discussed in Section 3.3. In Section 3.2, the dopant concentrations of the HTLs in the simulated PSCs are set to the optimized values.

3.2. Effect of Thickness of Absorbers and HTLs.

Because the band gaps of $CsSnI_3$ (E_g = 1.3 eV[10]), $CsGeI_3$ (E_g = 1.63 eV[10]), and $CsSn_{0.5}Ge_{0.5}I_3$ (E_g = 1.5 eV[10]), which are adopted as HTLs with p-type doping, are suitable for the solar spectrum, the photogenerated carriers are generated both in the absorbers and HTLs. The contour plots of the PV parameters PCE, V_{oc}, J_{sc}, and FF with the simultaneous variation of the absorber and HTL thickness of the simulated Sn−Ge-based all-inorganic PSCs are shown in Figure 5. Figure 5a shows the PV cell parameters for the TiO_2/i-$CsSnI_3$/p-$CsSnI_3$ cell with a N_A ($CsSnI_3$ HTL) of 10^{19} cm^{-3}. With a fixed thickness of $CsSnI_3$ HTL, the PCE decreases with the increase of $CsSnI_3$ absorber thickness on the whole. The maximum PCE is 28.35%, which occurs when the absorber is 0 nm and the HTL is 200 nm. The V_{oc} also decreases slightly with the increasing thickness of $CsSnI_3$ absorber. The simulated maximum PCE of 28.35% here for the n-TiO_2/p-$CsSnI_3$ cell is in agreement with other recent reports (30.17%).[33] The J_{sc} increases with increasing absorber thickness on the whole. The PV parameters for the TiO_2/i-$CsGeI_3$/p-$CsGeI_3$ with a N_A ($CsGeI_3$ HTL) of 10^{19} cm^{-3} and TiO_2/i-$CsSn_{0.5}Ge_{0.5}I_3$/p-$CsSn_{0.5}Ge_{0.5}I_3$ cells with a N_A ($CsSn_{0.5}Ge_{0.5}I_3$ HTL) of 10^{19} cm^{-3} are shown in Figure 5c,e, respectively, and the trends are similar to those of TiO_2/i-$CsSnI_3$/p-$CsSnI_3$ cells. The maximum PCE of TiO_2/i-$CsGeI_3$/p-$CsGeI_3$ cells is 17.49%, which occurs when the absorber is 0 nm and the HTL is 400 nm. The low performance of TiO_2/i-$CsGeI_3$/p-$CsGeI_3$ cells may be owing to the relatively low absorption coefficient in the visible light region of $CsGeI_3$. The maximum PCE of TiO_2/i-$CsSn_{0.5}Ge_{0.5}I_3$/p-$CsSn_{0.5}Ge_{0.5}I_3$ is 26.35%, which occurs when the absorber is 0 nm and the HTL is 800 nm. The best photovoltaic performance and optimal device parameters of the simulated Sn−Ge based all-inorganic PSCs cells are summarized in Table 2. From Figure 5 and Table 2, it could be concluded that the n-p structures could have better photovoltaic performance than the conventional n-i-p structures for the TiO_2/i-$CsSnI_3$/p-$CsSnI_3$, TiO_2/i-$CsGeI_3$/p-$CsGeI_3$, and TiO_2/i-$CsSn_{0.5}Ge_{0.5}I_3$/p-$CsSn_{0.5}Ge_{0.5}I_3$ PSCs if the defects in HTLs created by high doping can be effectively controlled. In comparison of our previous study[7] on the ETLs of $CsSnI_3$-based PSCs, it seems that the influence of HTLs on the PV performance is larger than that of ETLs for $CsSnI_3$-based PSCs (maybe also for all-inorganic $CsSn_xGe_{1-x}I_3$ based PSCs).

For the TiO_2/i-$CsSnI_3$/p-$CsGeI_3$ PSCs with a N_A ($CsGeI_3$ HTL) of 10^{19} cm^{-3} (Figure 5b), with a fixed thickness of $CsGeI_3$ HTL, the PCE increases first and then decrease slightly with the increasing thickness of $CsSnI_3$ absorber. The maximum PCE is 25.23%, which occurs when the $CsSnI_3$ absorber is 200 nm and the $CsGeI_3$ HTL is 50 nm. For the TiO_2/i-$CsGeI_3$/p-$CsSnI_3$ PSCs with a N_A ($CsSnI_3$ HTL) of 10^{19} cm^{-3} (Figure 5d), with a fixed thickness of $CsGeI_3$ absorber, the PCE decreases slightly with the increase of $CsSnI_3$ HTL thickness, due to the high recombination rate in the p-$CsSnI_3$ HTL region, and reaches the highest values with 50 nm HTL thickness. The PCE increases with the increase of $CsGeI_3$ absorber thickness and tends to be saturated (∼11.8%, not in Figure 5d) when the $CsGeI_3$ absorber is 600 nm and

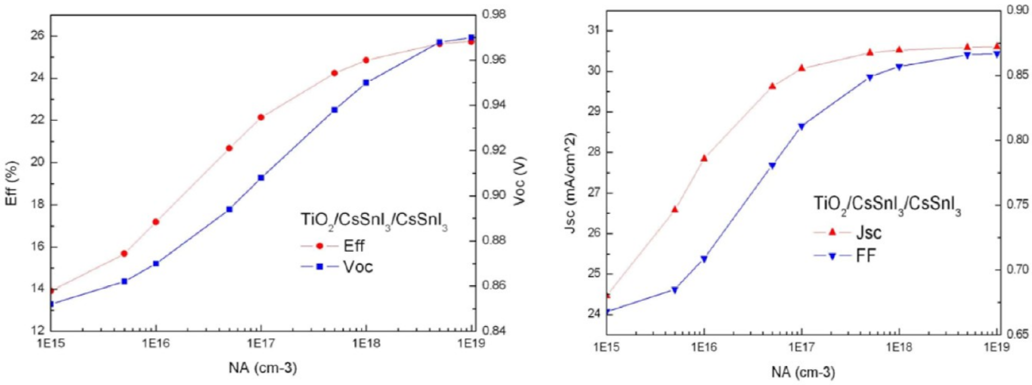

(a) $TiO_2/CsSnI_3/CsSnI_3$

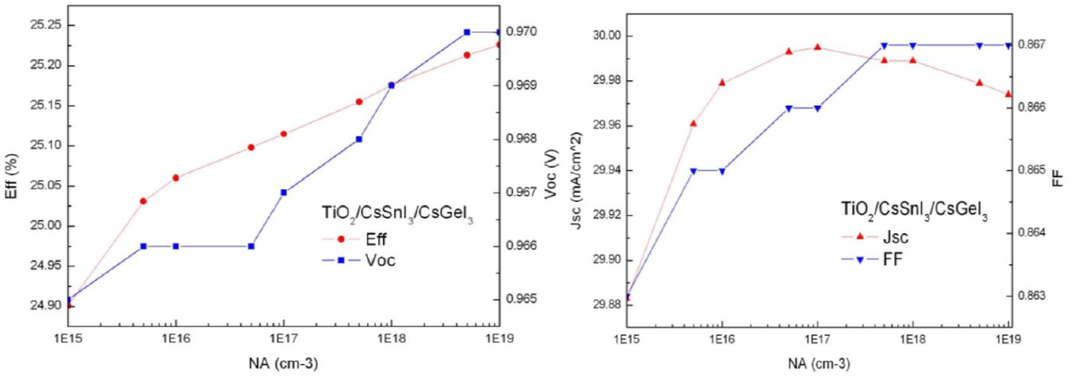

(b) $TiO_2/CsSnI_3/CsGeI_3$

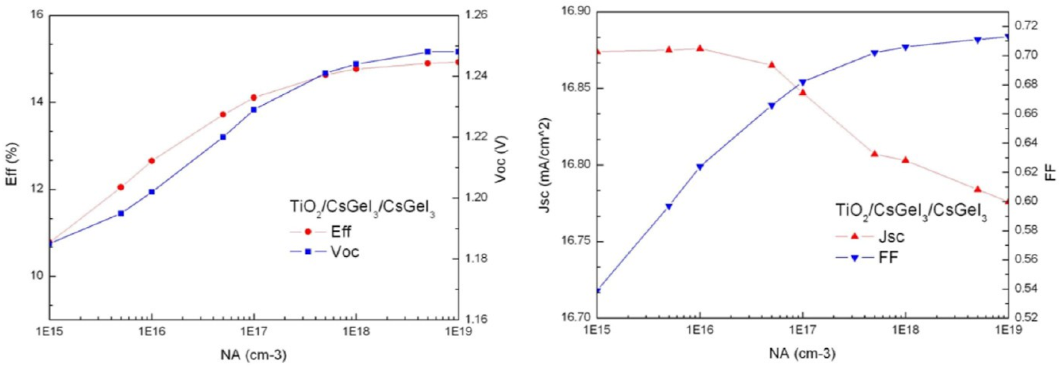

(c) $TiO_2/CsGeI_3/CsGeI_3$

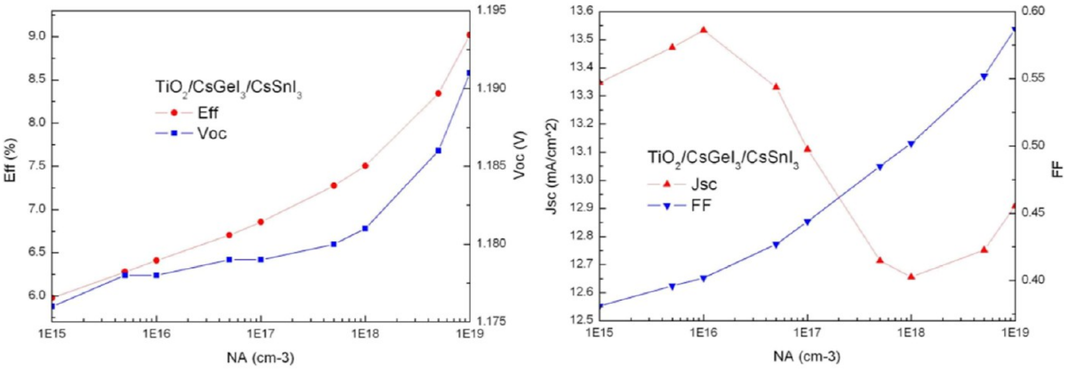

(d) $TiO_2/CsGeI_3/CsSnI_3$

Figure 4. continued

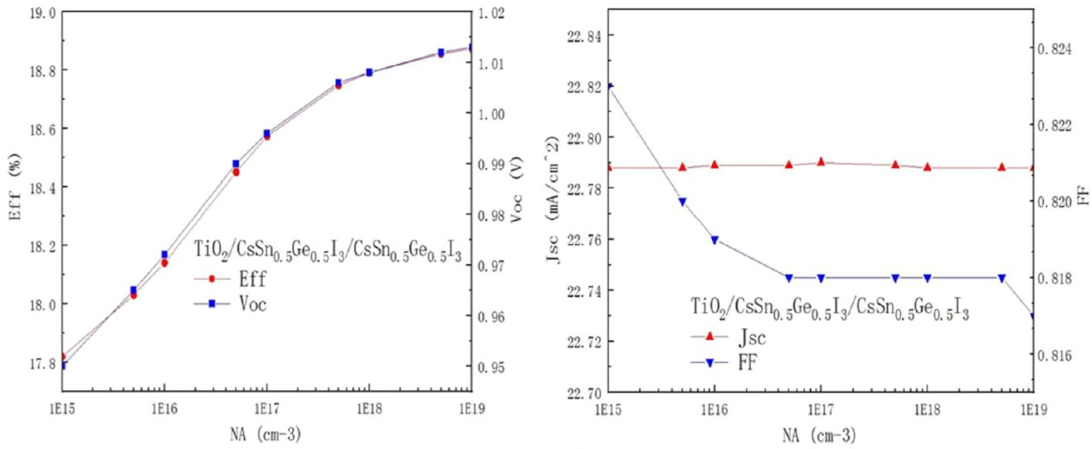

(e) $TiO_2/CsSn_{0.5}Ge_{0.5}I_3/CsSn_{0.5}Ge_{0.5}I_3$

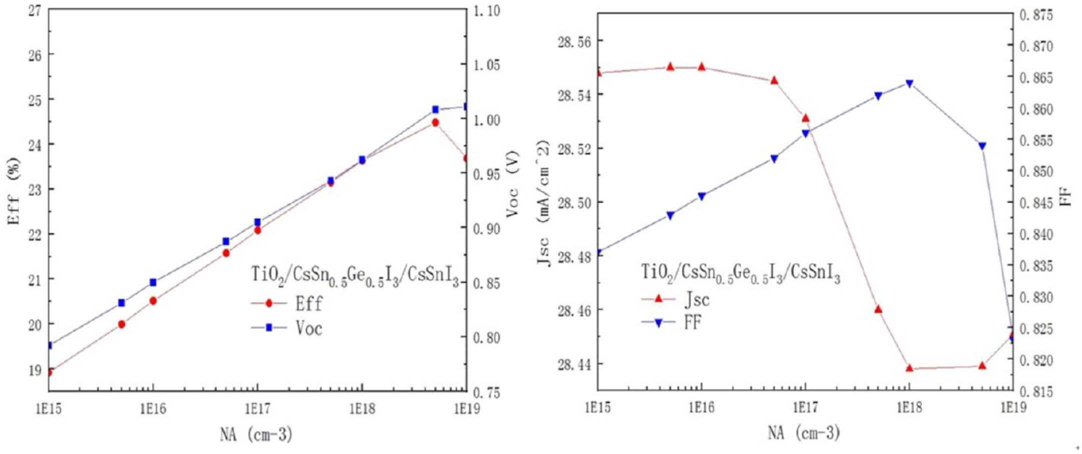

(f) $TiO_2/CsSn_{0.5}Ge_{0.5}I_3/CsSnI_3$

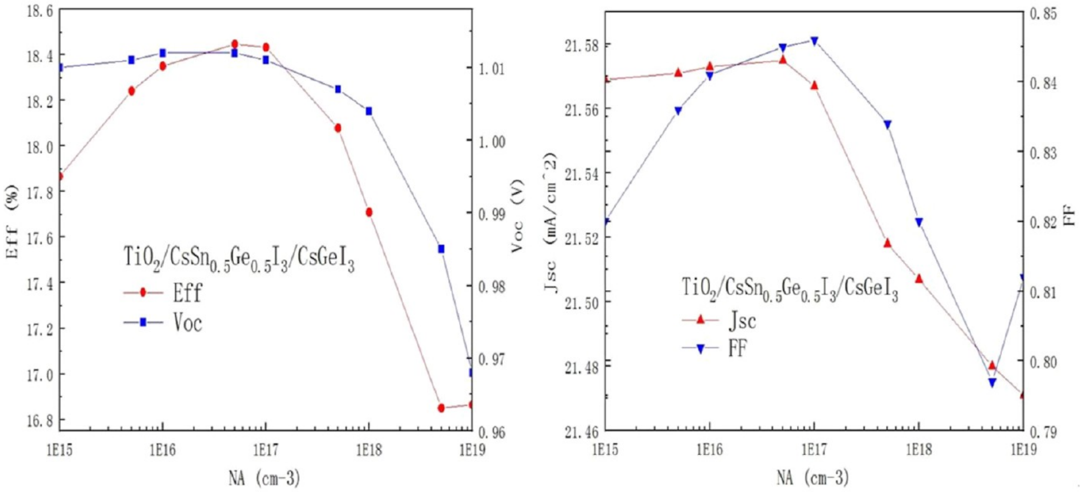

(g) $TiO_2/CsSn_{0.5}Ge_{0.5}I_3/CsGeI_3$

Figure 4. PV cell parameters as functions of acceptor concentrations (N_A) of HTLs. Left panel is efficiency [Eff (%)] and open circuit voltage (V_{oc} in V), and right panel is short-circuit current (J_{sc} in mA/cm^2) and FF of PV devices with different combinations of absorbers and HTLs. (a) $TiO_2/CsSnI_3/CsSnI_3$. (b) $TiO_2/CsSnI_3/CsGeI_3$. (c) $TiO_2/CsGeI_3/CsGeI_3$. (d) $TiO_2/CsGeI_3/CsSnI_3$. (e) $TiO_2/CsSn_{0.5}Ge_{0.5}I_3/CsSn_{0.5}Ge_{0.5}I_3$. (f) $TiO_2/CsSn_{0.5}Ge_{0.5}I_3/CsSnI_3$. (g) $TiO_2/CsSn_{0.5}Ge_{0.5}I_3/CsGeI_3$.

$CsSnI_3$ HTL is 50 nm. The V_{oc} almost keeps constant ~1.19 V. For the TiO_2/i-$CsSn_{0.5}Ge_{0.5}I_3/p$-$CsSnI_3$ PSCs with a N_A ($CsSnI_3$ HTL) of 5×10^{18} cm^{-3} (Figure 5f), with a fixed thickness of $CsSnI_3$ HTL, the PCE decreases with the increase of $CsSn_{0.5}Ge_{0.5}I_3$ absorber thickness on the whole. The maximum PCE is 25.84%, which occurs when the $CsSn_{0.5}Ge_{0.5}I_3$ absorber is 50 nm (0 nm deducted) and the $CsSnI_3$ HTL is 200 nm. The contours of V_{oc} are approximately circular arc and decrease slightly with the increasing thickness of absorber and HTL. For the TiO_2/i-$CsSn_{0.5}Ge_{0.5}I_3/p$-$CsGeI_3$

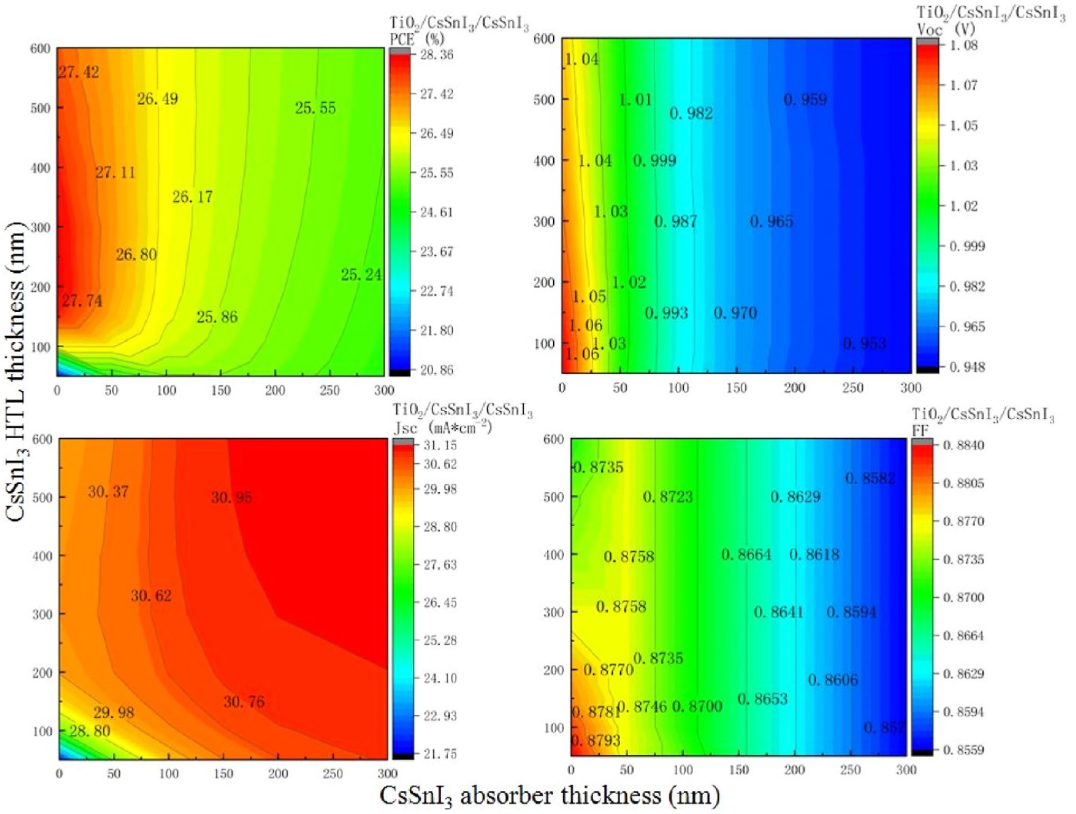

(a) $TiO_2/CsSnI_3/CsSnI_3$

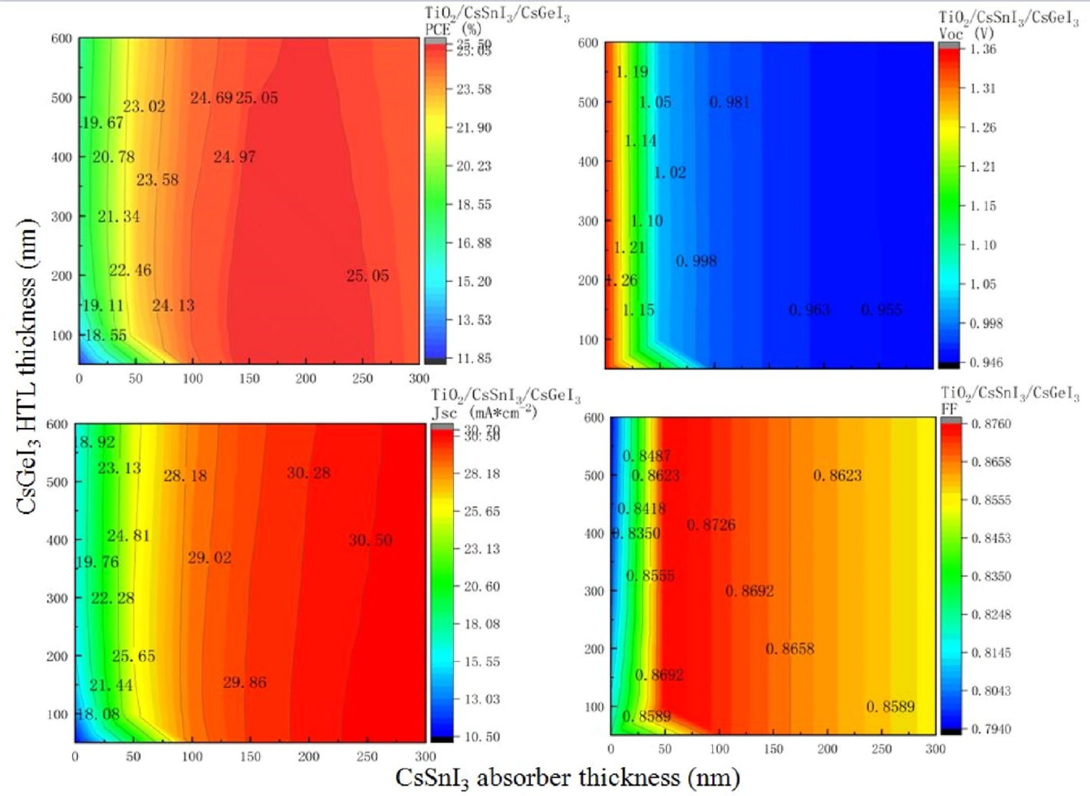

(b) $TiO_2/CsSnI_3/CsGeI_3$

Figure 5. continued

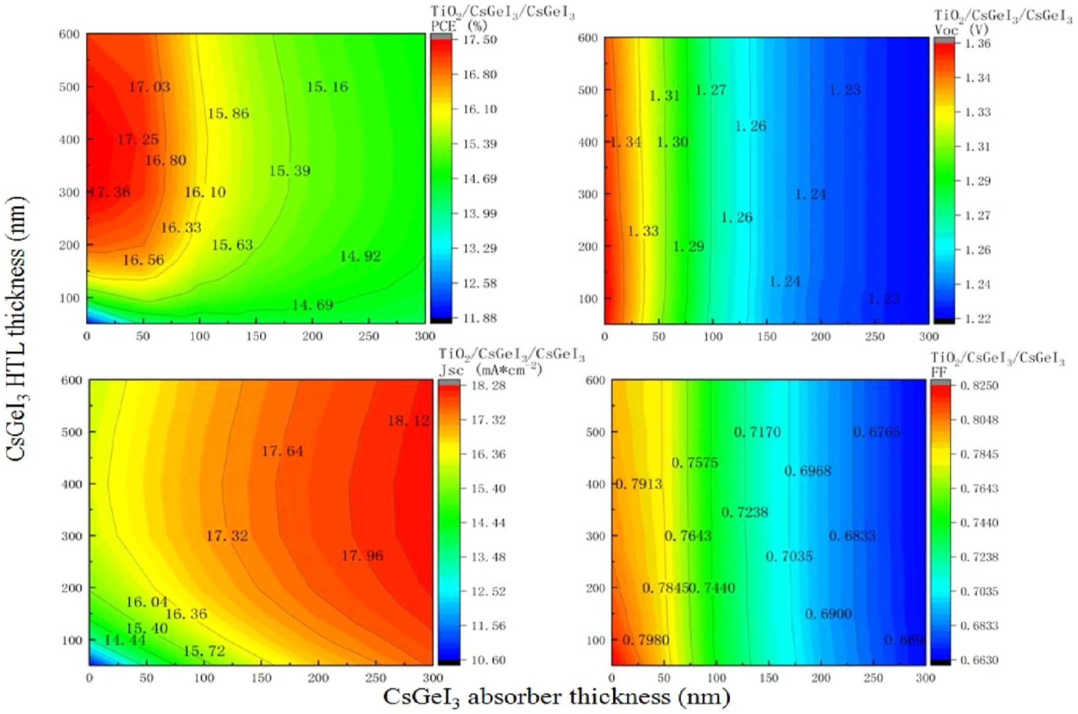

(c) $TiO_2/CsGeI_3/CsGeI_3$

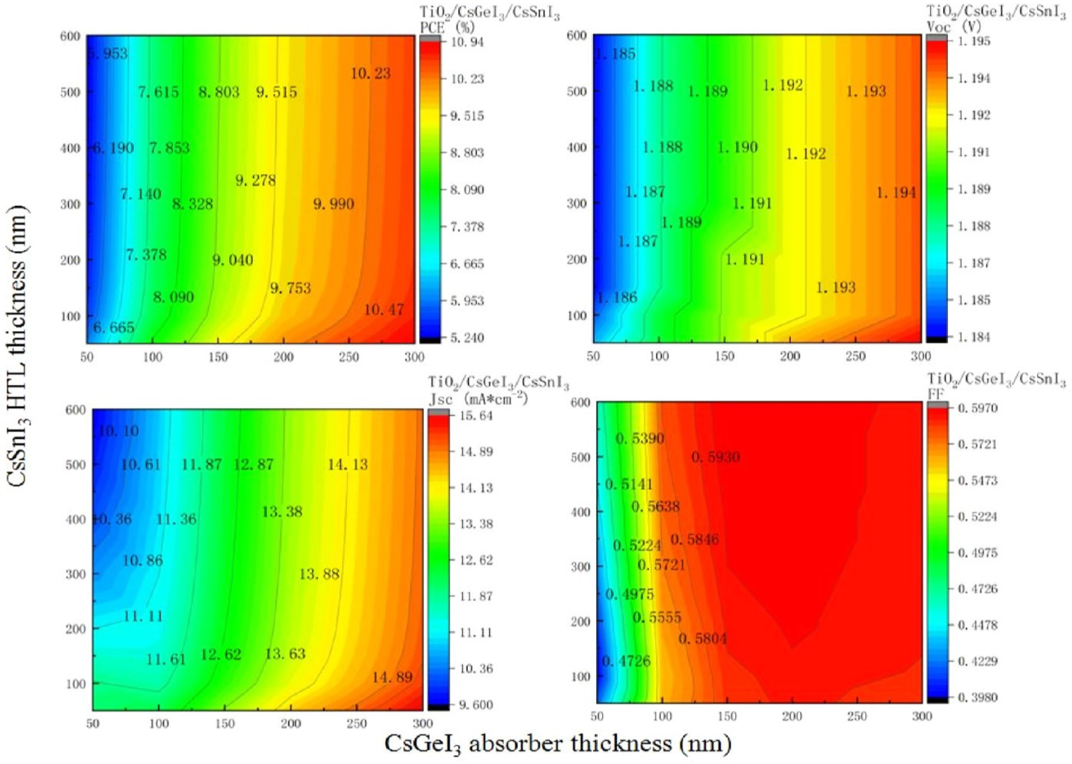

(d) $TiO_2/CsGeI_3/CsSnI_3$

Figure 5. continued

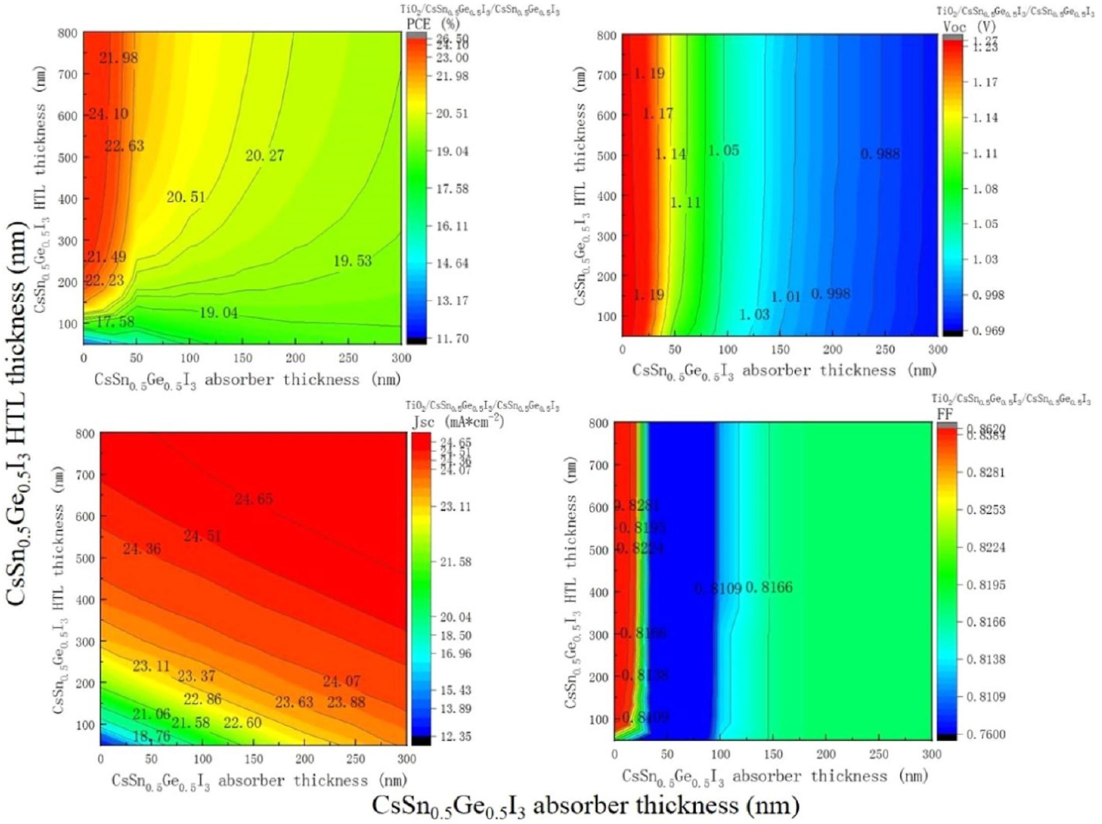

(e) TiO$_2$/CsSn$_{0.5}$Ge$_{0.5}$I$_3$/CsSn$_{0.5}$Ge$_{0.5}$I$_3$

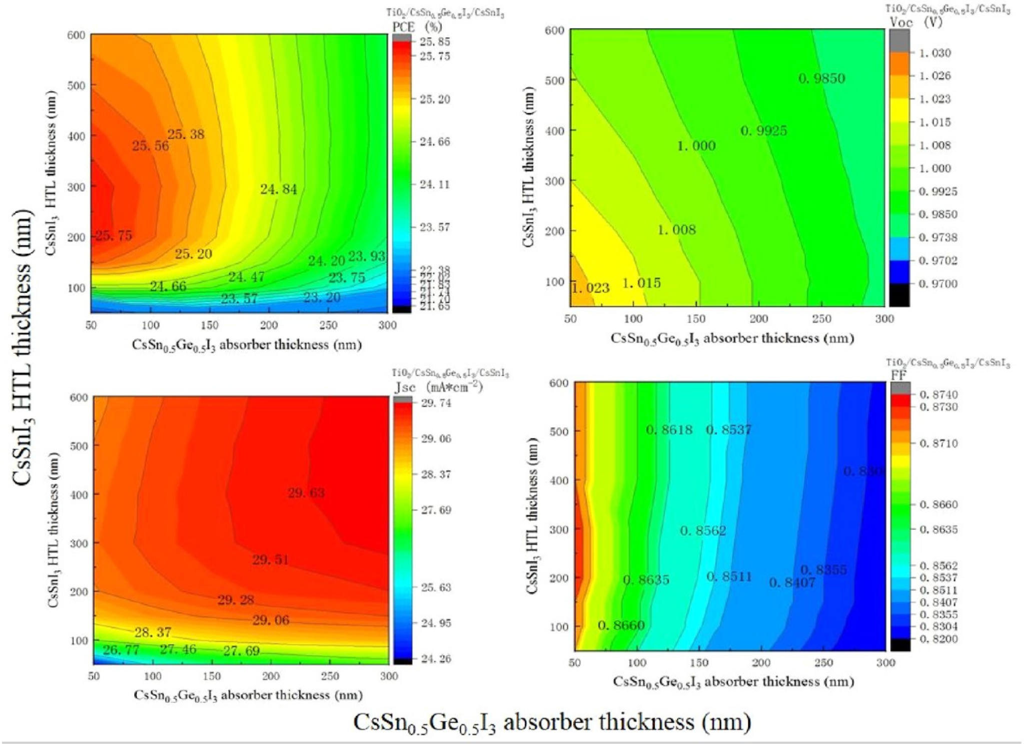

(f)TiO$_2$/CsSn$_{0.5}$Ge$_{0.5}$I$_3$/CsSnI$_3$

Figure 5. continued

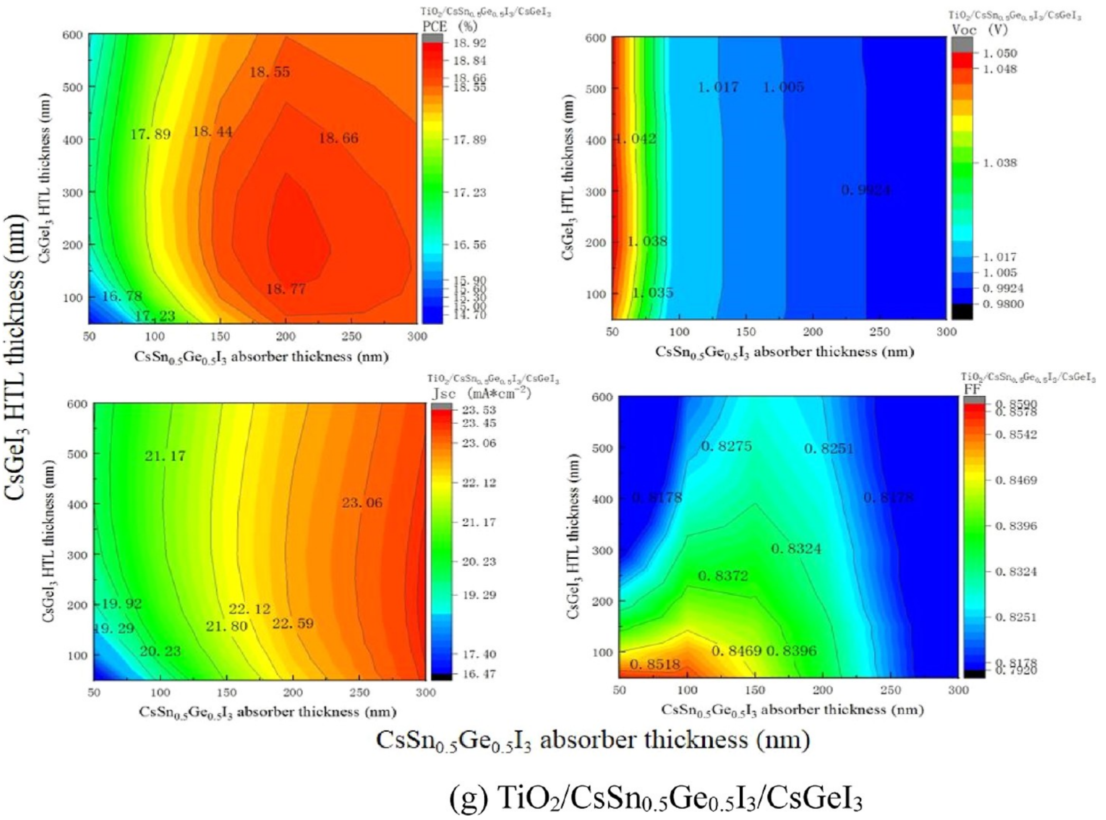

Figure 5. Contour plots showing the variation of PCE, V_{oc}, J_{sc}, and FF with simultaneous variation of the thickness of absorber and HTL for $TiO_2/CsSnI_3/CsSnI_3$ (a), $TiO_2/CsSnI_3/CsGeI_3$ (b), $TiO_2/CsGeI_3/CsGeI_3$ (c), $TiO_2/CsGeI_3/CsSnI_3$ (d), $TiO_2/CsSn_{0.5}Ge_{0.5}I_3/CsSn_{0.5}Ge_{0.5}I_3$ (e), $TiO_2/CsSn_{0.5}Ge_{0.5}I_3/CsSnI_3$ (f), and $TiO_2/CsSn_{0.5}Ge_{0.5}I_3/CsGeI_3$ (g).

Table 2. Best Photovoltaic Performance and Optimal Device Parameters of Sn–Ge-based All-Inorganic PSCs

PSC	$TiO_2/CsSnI_3/CsSnI_3$	$TiO_2/CsSnI_3/CsGeI_3$	$TiO_2/CsGeI_3/CsGeI_3$	$TiO_2/CsGeI_3/CsSnI_3$	$TiO_2/CsSn_{0.5}Ge_{0.5}I_3/CsSn_{0.5}Ge_{0.5}I_3$	$TiO_2/CsSn_{0.5}Ge_{0.5}I_3/CsSnI_3$	$TiO_2/CsSn_{0.5}Ge_{0.5}I_3/CsGeI_3$
thickness of absorber (nm)	0	200	0	600	0	50 (deduct 0)	200
thickness of HTL (nm)	200	50	400	50	800	200	200
acceptor concentration in HTL N_A (cm^{-3})	10^{19}	10^{19}	10^{19}	10^{19}	10^{19}	5×10^{18}	5×10^{16}
Eff (%)	28.35	25.23	17.49	11.79	26.35	25.84	18.83
V_{oc} (V)	1.075	0.961	1.353	1.197	1.243	1.020	1.000
J_{sc} ($mA{\cdot}cm^{-2}$)	30.002	30.421	16.191	16.930	24.600	29.035	22.634
FF	0.879	0.863	0.799	0.582	0.861	0.873	0.832

PSCs with a N_A ($CsGeI_3$ HTL) of 5×10^{16} cm^{-3} (Figure 5g), with a fixed thickness of $CsGeI_3$ HTL, the PCE increases first and then decreases slightly with the increasing thickness of the $CsSn_{0.5}Ge_{0.5}I_3$ absorber. The maximum PCE is 18.83%, which occurs when the $CsSn_{0.5}Ge_{0.5}I_3$ absorber is 200 nm and $CsGeI_3$ HTL is 200 nm.

In order to seek the relation between cell performance and thickness of absorber and HTL further, it will be desirable to perform quantitative or semiquantitative analysis. Following the practice of fitting simulation results with analytical functions in strained functional materials,[34−36] here, we adapted analytical functions with a combination of polynomials for efficiencies as functions of thickness of absorber (x) and HTL (y). Such analytical functions are fitted from Figure 5 and listed as following

$TiO_2/i\text{-}CsSnI_3/p\text{-}CsSnI_3$:

$$F_1(x, y) = (-175.06047 + 45.62165x + 10.66937y - 0.01457y^2 + 5.20429 \times 10^{-6}y^3) /(1 + 1.70742x + 6.37409 \times 10^{-4}x^2 - 7.53982 \times 10^{-7}x^3 + 0.30398y - 2.98576 \times 10^{-4}y^2) \tag{6}$$

$TiO_2/i\text{-}CsSnI_3/p\text{-}CsGeI_3$:

$$F_2(x, y) = (6.86938 + 0.91395x + 0.19256y - 3.07522 \times 10^{-4}y^2 + 1.19329 \times 10^{-7}y^3) /(1 + 0.02766x + 3.26208 \times 10^{-5}x^2 - 3.3202 \times 10^{-8}x^3 + 0.00652y - 7.54361 \times 10^{-6}y^2) \tag{7}$$

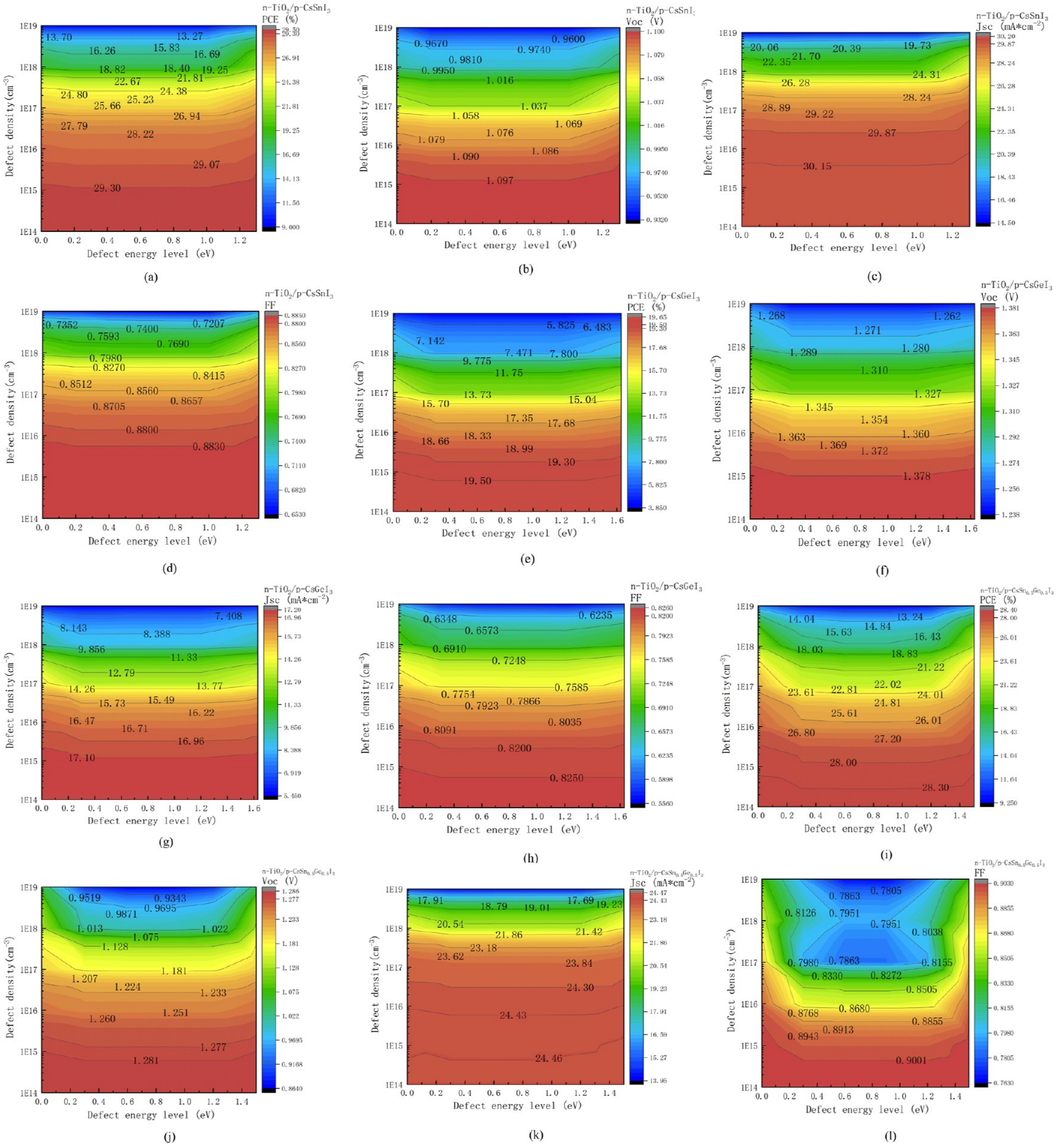

(a) (b) (c) (d) (e) (f) (g) (h) (i) (j) (k) (l)

Figure 6. Contour plots showing the variation of PCE, V_{oc}, J_{sc}, and FF with simultaneous variation of the defect density and defect energy level for n-TiO$_2$/p-CsSnI$_3$ (a–d), n-TiO$_2$/p-CsGeI$_3$ (e–h), and n-TiO$_2$/p-CsSn$_{0.5}$Ge$_{0.5}$I$_3$ (i–l) PSCs.

TiO$_2$/i-CsGeI$_3$/p-CsGeI$_3$

$$F_3(x, y) = (5.72187 + 0.59x + 0.23566y - 4.2 \times 10^{-4}y^2 + 1.6987 \times 10^{-7}y^3)/(1 + 0.03373x + 5.39156 \times 10^{-5}x^2 - 9.8699 \times 10^{-8}x^3 + 0.00823y - 1.12611 \times 10^{-5}y^2) \quad (8)$$

TiO$_2$/i-CsGeI$_3$/p-CsSnI$_3$:

$$F_4(x, y) = (2.50842 + 0.12262x - 0.00998y + 3.08012 \times 10^{-5}y^2 - 2.96033 \times 10^{-8}y^3)/(1 + 0.00655x + 1.0788 \times 10^{-5}x^2 - 1.4497 \times 10^{-8}x^3 + 4.90165 \times 10^{-4}y - 6.54653 \times 10^{-7}y^2) \quad (9)$$

$TiO_2/i\text{-}CsSn_{0.5}Ge_{0.5}I_3/p\text{-}CsSn_{0.5}Ge_{0.5}I_3$:

$$\begin{aligned}F_5(x, y) = {} & (-3.154 + 1.8x + 0.51y - 5.874 \times 10^{-4}y^2 \\ & + 1.755 \times 10^{-7}y^3)/(1 + 0.107x - 1.043 \times 10^{-4}x^2 \\ & + 2.211 \times 10^{-7}x^3 + 0.0135y - 1.145 \times 10^{-5}y^2) \quad (10)\end{aligned}$$

$TiO_2/i\text{-}CsSn_{0.5}Ge_{0.5}I_3/p\text{-}CsSnI_3$:

$$\begin{aligned}F_6(x, y) = {} & (35.466 - 0.432x - 0.942y + 1.27 \times 10^{-3}y^2 \\ & - 2.602 \times 10^{-7}y^3)/(1 - 0.0168x - 5.944\times10^{-6}x^2 \\ & - 5.718 \times 10^{-9}x^3 - 0.0326y + 3.756 \times 10^{-5}y^2) \quad (11)\end{aligned}$$

$TiO_2/i\text{-}CsSn_{0.5}Ge_{0.5}I_3/p\text{-}CsGeI_3$:

$$\begin{aligned}F_7(x, y) = {} & (1.637 + 0.376x + 0.318y - 4.366 \times 10^{-4}y^2 \\ & + 8.501 \times 10^{-8}y^3)/(1 + 0.0123x + 2.112 \times 10^{-5}x^2 \\ & - 1.146 \times 10^{-8}x^3 + 0.0154y - 1.802 \times 10^{-5}y^2) \quad (12)\end{aligned}$$

where $F_1(x, y)$, $F_2(x, y)$, $F_3(x, y)$, $F_4(x, y)$, $F_5(x, y)$, $F_6(x, y)$, and $F_7(x, y)$ are the efficiencies as functions of the thickness of absorber (x) and HTL (y) for the $TiO_2/i\text{-}CsSnI_3/p\text{-}CsSnI_3$, $TiO_2/i\text{-}CsSnI_3/p\text{-}CsGeI_3$, $TiO_2/i\text{-}CsGeI_3/p\text{-}CsGeI_3$, $TiO_2/CsGeI_3/CsSnI_3$, $TiO_2/CsSn_{0.5}G_{e0.5}I_3/CsSn_{0.5}Ge_{0.5}I_3$, $TiO_2/CsSn_{0.5}Ge_{0.5}I_3/CsSnI_3$, and $TiO_2/CsSn_{0.5}Ge_{0.5}I_3/CsGeI_3$ cells, respectively. From the function expressions (6–12), it could be found that the efficiencies as functions of the thickness of absorber and HTL can be expressed as the forms of polynomial division for all the simulated all-inorganic $CsSn_xGe_{1-x}I_3$-based PSCs. The detailed function fitting results (comparison of the original and function fitting contour plots and scatter plots) are presented in Figure S2 in the Supporting Information.

3.3. Effect of Defects in HTLs and Interface Trap. In our previous study,[7] the several ETLs of $CsSnI_3$-based PSCs were optimized and the $TiO_2/CsSnI_3$/spiro-MeOTAD cell with the acceptor concentration of $CsSnI_3$ absorber being 5 × 10^{17} cm^{-3} could exhibit the efficiency of 20.2%, in which the thickness and acceptor concentration of spiro-MeOTAD were 400 nm and 3 × 10^{17} cm^{-3} (according to the ref 37), respectively. When the thickness and acceptor concentration of spiro-MeOTAD were 200 nm and 1 × 10^{18} cm^{-3}, respectively, the $TiO_2/CsSnI_3$/spiro-MeOTAD cell could exhibit the much higher efficiency of 24.1% with a V_{oc} of 0.967 V without considering the effects of defects created by the high doping in HTLs in the simulation. Experimental study[38,39] has revealed the interplay between the PSC device photovoltaic performance and its reproducibility: a thin spiro-MeOTAD HTL improves the photovoltaic performances of the devices while reducing their reproducibility. Higher doping in HTLs can create deep coulomb traps, which could have significant recombination effects on the photogenerated carriers and decrease charge carrier mobility. Our simulated theoretical efficiency (24.1% with the acceptor concentration of spiro-MeOTAD being 1 × 10^{18} cm^{-3}) for the $TiO_2/CsSnI_3$/spiro-MeOTAD cell agrees well with other recent simulation reports.[37,40,41] Ravidas et al.[41] simulated the FTO/TiO2/$CsSnI_3$/spiro-MeOTAD/Au cell (the acceptor concentration of spiro-MeOTAD is 1 × 10^{19} cm^{-3}) using SCAPS-1D, and the cell exhibited the highest PCE of 25.18%. Srivastava et al.[42] simulated the FTO/PCBM/$CsSnI_3$/PTAA/Au cell using SCAPS-1D, and the cell showed the even higher PCE of 28.97% with very high acceptor concentration of $CsSnI_3$ absorber (~5 × 10^{20} cm^{-3}). Under the condition of high acceptor concentration of $CsSnI_3$ absorber, e.g., about 1 × 10^{19} cm^{-3}, our simulated PCE of $TiO_2/CsSnI_3$/spiro-MeOTAD cell can be also as high as 28.14%. Different simulation work may be performed under different assumptions, but in comparison of the ref 42, the trend of PCE in terms of acceptor concentration of $CsSnI_3$ absorber is similar. Caution should be noted that PSCs with acceptor concentrations of $CsSnI_3$ that are too high may create many deep Coulomb traps and increase the recombination rate, which may reduce the performance of realistic devices. The $TiO_2/CsGeI_3$/spiro-MeOTAD cell with the acceptor concentration of $CsGeI_3$ absorber being 1 × 10^{19} cm^{-3} is simulated and could exhibit the efficiency of 17.98% and V_{oc} of 1.36 V, in which the thickness and acceptor concentration of spiro-MeOTAD were 200 nm and 1 × 10^{18} cm^{-3}, respectively. The photovoltaic performance is slightly higher than that of the optimized $n\text{-}TiO_2/p\text{-}CsGeI_3$ cell (17.49%), but as is known, spiro-MeOTAD is very expensive and the complexity of device processes increases. The $TiO_2/CsSn_{0.5}Ge_{0.5}I_3$/spiro-MeOTAD cell with the acceptor concentration of $CsSn_{0.5}Ge_{0.5}I_3$ absorber being 1 × 10^{19} cm^{-3} is simulated and could exhibit the efficiency of 26% and V_{oc} of 1.242 V, in which the thickness and acceptor concentration of spiro-MeOTAD were 200 nm and 1 × 10^{18} cm^{-3}, respectively. The photovoltaic performance is slightly lower than that of the optimized $n\text{-}TiO_2/p\text{-}CsSn_{0.5}Ge_{0.5}I_3$ cell (26.35%).

In this section, the impact of defect level positions and defect densities in HTLs on the performance of PSCs are simulated, focusing on how variations in these parameters affect carrier recombination and overall efficiency. The DOS model in AMPS is used in this simulation. The contour plots of the PV parameters with the simultaneous variation of defect density and defect energy levels for the $n\text{-}TiO_2/p\text{-}CsSnI_3$, $n\text{-}TiO_2/p\text{-}CsGeI_3$, and $n\text{-}TiO_2/p\text{-}CsSn_{0.5}Ge_{0.5}I_3$ PSCs (the optimal device parameters are in Table 2) are shown in Figure 6. The energy distribution is Gaussian and the characteristic energy is 0.1 eV.[43,44] The electron and hole capture cross section is set to 10^{-15} cm^2.[41,43,44] The defect density is set from 10^{14} to 10^{19} cm^{-3} and the defect energy levels (above the valence band edge) are set from 0 eV to the band gaps of perovskites. The main reason for the defects in the perovskite layers is the corrupt quality of doping level and the process of doping in perovskites.[41] The recombination process is explained by the Shockley-Read-Hall (SRH) recombination model[41] and the DOS model in AMPS is used in this section.

From Figure 6, we can observe that the nature of variation of the PV parameters is almost similar for all the simulated PSCs. The difference lies in the range of the values of the PV parameters. The PCE of PSCs drastically reduces from 29.40 to 9.08%, 19.61 to 3.86%, and 28.38 to 9.28% for the $n\text{-}TiO_2/p\text{-}CsSnI_3$, $n\text{-}TiO_2/p\text{-}CsGeI_3$, and $n\text{-}TiO_2/p\text{-}CsSn_{0.5}Ge_{0.5}I_3$ PSCs, respectively, as the defect density is increased from 10^{14} to 10^{19} cm^{-3} and the defect energy levels vary from 0 eV to the band gaps of perovskites. The V_{oc} of PSCs decreases (slightly) from 1.1 to 0.932 V, 1.381 to 1.238 V, and 1.285 to 0.864 for the $n\text{-}TiO_2/p\text{-}CsSnI_3$, $n\text{-}TiO_2/p\text{-}CsGeI_3$, and $n\text{-}TiO_2/p\text{-}CsSn_{0.5}Ge_{0.5}I_3$ PSCs, respectively, with the same variation in the defect density and defect energy levels. The J_{sc} of PSCs decreases from 30.198 to 14.525 mA*cm^{-2}, 17.184 to 5.479 mA*cm^{-2}, and 24.461 to 13.953 mA*cm^{-2} for the $n\text{-}TiO_2/p\text{-}CsSnI_3$, $n\text{-}TiO_2/p\text{-}CsGeI_3$, and $n\text{-}TiO_2/p\text{-}CsSn_{0.5}Ge_{0.5}I_3$ PSCs, respectively. The FF of PSCs decreases from 0.885 to 0.653,

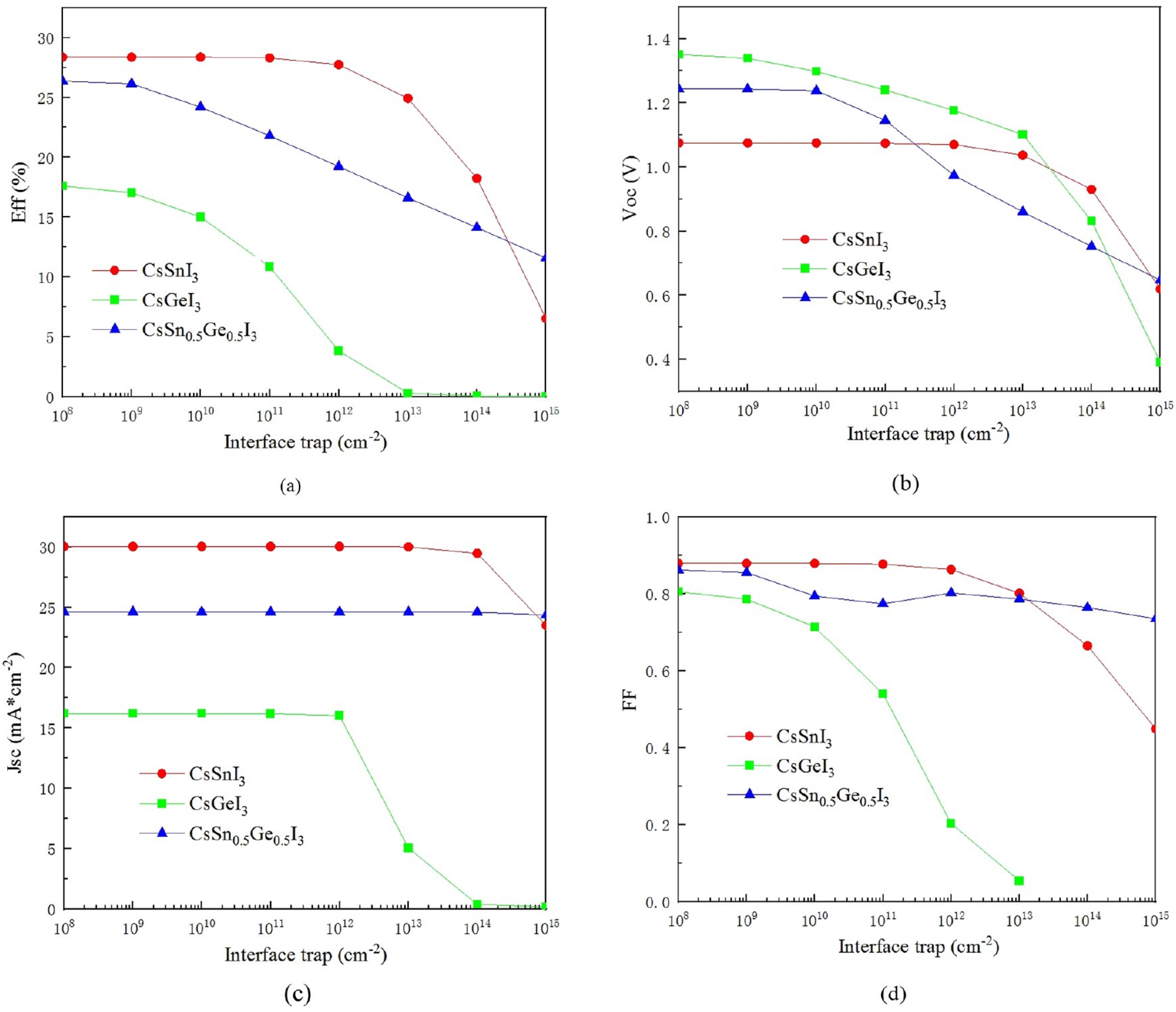

Figure 7. Photovoltaic parameters of n-TiO$_2$/p-CsSnI$_3$, n-TiO$_2$/p-CsGeI$_3$, and n-TiO$_2$/p-CsSn$_{0.5}$Ge$_{0.5}$I$_3$ PSCs as functions of the interface trap density Eff (a), V_{oc} (b), J_{sc} (c), and FF (d).

0.826 to 0.556, and 0.903 to 0.763 for the n-TiO$_2$/p-CsSnI$_3$, n-TiO$_2$/p-CsGeI$_3$, and n-TiO$_2$/p-CsSn$_{0.5}$Ge$_{0.5}$I$_3$ PSCs, respectively. It is found that the influence of defect density on the PV performance is larger than that of defect level position. The devices could maintain high PCE for defect density below about 5×10^{17} cm^{-3}. Defect energy levels close to the middle of band gaps of perovskites have larger recombination influence on the PV performance than that of defect levels at the edge of band gaps, which is consistent with the SRH recombination model.

In the device simulation, the effects of the interface trap on the performance of PSCs are also studied by introducing 5 nm interface defect layers at the TiO$_2$/perovskite interfaces for the n-TiO$_2$/p-CsSnI$_3$, n-TiO$_2$/p-CsGeI$_3$, and n-TiO$_2$/p-CsSn$_{0.5}$Ge$_{0.5}$I$_3$ PSCs. The electron and hole capture cross section is set to 10^{-15} cm^2.[41,43,44] Figure 7 shows the plot of PV cell parameters as functions of the interface trap density. From the figure, the interface trap has an important influence on efficiency, V_{oc}, J_{sc}, and FF. It is clear that efficiency, V_{oc}, J_{sc}, and FF decrease with increasing interface trap density. For n-TiO$_2$/p-CsSnI$_3$ cells, when the interface trap densities are 10^8 and 10^{12} cm^{-2}, the efficiencies decrease slowly (~28.3%). However, when the interface trap increases to 10^{12} and 10^{14} cm^{-2}, the efficiency decreases sharply to 27.74 and 6.53%, respectively. For n-TiO$_2$/p-CsGeI$_3$ cells, when the interface trap densities are 10^8 and 10^{13} cm^{-2}, the efficiencies decrease sharply from ~17.5 to 0.3%. Especially, the FF decreases sharply from ~0.8 to 0.05 when the interface trap densities are 10^8 and 10^{13} cm^{-2}. For n-TiO$_2$/p-CsSn$_{0.5}$Ge$_{0.5}$I$_3$ cells, when the interface trap densities are 10^8 and 10^{15} cm^{-2}, the efficiencies decrease from 26.36 to 11.58%. From the simulation results, it seems that the performance of PSCs with a larger perovskite band gap is more sensitive to the interface trap density. Interface trap density increases the recombination centers and hence change in shunt resistance. Optimizing the doping of the ETL and the formation of a flat, smooth, and homogeneous surface will significantly reduce the interface trap density and hence enhance the performance. The recombination mechanisms of photocarriers at the ETL/perovskite interfaces could be found in the literature, such as refs 45 and 46.

4. CONCLUSIONS

$CsSnI_3$, $CsGeI_3$, and $CsSn_{0.5}Ge_{0.5}I_3$ are used both as all-inorganic lead-free absorbers and as HTLs with *p*-type doping for PSCs. Effects of the dopant concentration of HTLs, the thickness of absorbers, and HTLs on the photovoltaic performance of PSCs are investigated to optimize the device structures. The optimized acceptor concentrations in HTLs are 10^{19} cm^{-3} for the TiO_2/*i*-$CsSnI_3$/*p*-$CsSnI_3$, TiO_2/*i*-$CsSnI_3$/*p*-$CsGeI_3$, TiO_2/*i*-$CsGeI_3$/*p*-$CsGeI_3$, TiO_2/*i*-$CsGeI_3$/*p*-$CsSnI_3$, and TiO_2/*i*-$CsSn_{0.5}Ge_{0.5}I_3$/*p*-$CsSn_{0.5}Ge_{0.5}I_3$ cells and the optimized acceptor concentrations in HTLs for TiO_2/*i*-$CsSn_{0.5}Ge_{0.5}I_3$/*p*-$CsSnI_3$ and TiO_2/*i*-$CsSn_{0.5}Ge_{0.5}I_3$/*p*-$CsGeI_3$ cells are 5×10^{18} and 5×10^{16} cm^{-3}, respectively. The maximum efficiencies from high to low are 28.35%, 26.35%, 25.84%, 25.23%, 18.83%, 17.49%, and 11.79% for the TiO_2/*i*-$CsSnI_3$/*p*-$CsSnI_3$, TiO_2/*i*-$CsSn_{0.5}Ge_{0.5}I_3$/*p*-$CsSn_{0.5}Ge_{0.5}I_3$, TiO_2/*i*-$CsSn_{0.5}Ge_{0.5}I_3$/*p*-$CsSnI_3$, TiO_2/*i*-$CsSnI_3$/*p*-$CsGeI_3$, TiO_2/*i*-$CsSn_{0.5}Ge_{0.5}I_3$/*p*-$CsGeI_3$, TiO_2/*i*-$CsGeI_3$/*p*-$CsGeI_3$, and TiO_2/*i*-$CsGeI_3$/*p*-$CsSnI_3$, respectively. The TiO_2/*i*-$CsGeI_3$/*p*-$CsSnI_3$ cell exhibits the lowest efficiency, 11.79%, in all of the simulated PSCs due to the spike-like band offset and low built-in electric field at the *i*-$CsGeI_3$/*p*-$CsSnI_3$ interface which leads to high recombination rate in the *p*-$CsSnI_3$ region ($>10^{21}$ s^{-1} cm^{-3}) and the low J_{sc}. It could be concluded that the *n-p* structures could have better photovoltaic performance than the conventional *n-i-p* structures for the TiO_2/*i*-$CsSnI_3$/*p*-$CsSnI_3$, TiO_2/*i*-$CsGeI_3$/*p*-$CsGeI_3$, and TiO_2/*i*-$CsSn_{0.5}Ge_{0.5}I_3$/*p*-$CsSn_{0.5}Ge_{0.5}I_3$ PSCs if the defects in HTLs created by high doping can be effectively controlled. In comparison to our previous study on the ETLs of $CsSnI_3$-based PSCs, it seems that the influence of HTLs on the PV performance is larger than that of ETLs for $CsSnI_3$-based PSCs (maybe also for all-inorganic $CsSn_xGe_{1-x}I_3$-based PSCs).

The effects of defect level position and defect density in HTLs on the performance of PSCs are simulated for the optimal *n*-TiO_2/*p*-$CsSnI_3$, *n*-TiO_2/*p*-$CsGeI_3$, and *n*-TiO_2/*p*-$CsSn_{0.5}Ge_{0.5}I_3$ PSCs. The PCE of PSCs drastically reduces from 29.40 to 9.08%, 19.61 to 3.86%, and 28.38 to 9.28% for the *n*-TiO_2/*p*-$CsSnI_3$, *n*-TiO_2/*p*-$CsGeI_3$, and *n*-TiO_2/*p*-$CsSn_{0.5}Ge_{0.5}I_3$ PSCs, respectively, as the defect density is increased from 10^{14} to 10^{19} cm^{-3} and the defect energy levels vary from 0 eV (above the valence band edge) to the band gaps of perovskites. It is found that the influence of defect density on the PV performance is larger than that of defect level position. The devices could maintain high PCE for defect density below about 5×10^{17} cm^{-3}. Defect energy levels close to the middle of band gaps of perovskites have larger recombination influence on the PV performance than that of defect levels at the edge of band gaps, which is consistent with the SRH recombination model. Furthermore, the increase of interface trap density is found to reduce the photovoltaic performance of PSCs.

We have examined throughout various factors that may have impacts on the photovoltaic performance of $CsSn_xGe_{1-x}I_3$-based PSCs. The insight gained in this work may be useful for the optimal design of $CsSn_xGe_{1-x}I_3$-based PSCs.

■ ASSOCIATED CONTENT

Supporting Information

The Supporting Information is available free of charge at https://pubs.acs.org/doi/10.1021/acs.energyfuels.4c03960.

Material parameters used in the simulation, energy band alignment of all-inorganic Sn−Ge-based perovskite and contact materials adopted in this study, comparison of the original and function fitting contour plots, and comparison of simulation and experimental *J*−*V* curves of FTO/PCBM (20 nm)/$CsSn_{0.5}Ge_{0.5}I_3$ (200 nm)/Spiro-OMeTAD PSCs (PDF)

■ AUTHOR INFORMATION

Corresponding Author

Jin-Cheng Zheng − *Collaborative Innovation Center for Optoelectronic Semiconductors and Efficient Devices, Department of Physics, Xiamen University, Xiamen 361005, China; Department of Physics and Department of New Energy Science and Engineering, Xiamen University Malaysia, Sepang 43900 Selangor, Malaysia*; Email: jczheng@xmu.edu.cn

Authors

Shuo Lin − *Key Laboratory of Light Field Manipulation and System Integration Applications in Fujian Province, School of Physics and Information Engineering, Minnan Normal University, Zhangzhou 363000, China*; orcid.org/0000-0003-0359-6439

Baoping Zhang − *Department of Microelectronics and Integrated Circuits, School of Electronic Science and Engineering, Xiamen University, Xiamen 361005, China*

Weichao Wang − *Collaborative Innovation Center for Optoelectronic Semiconductors and Efficient Devices, Department of Physics, Xiamen University, Xiamen 361005, China*

Tie-Yu Lü − *Collaborative Innovation Center for Optoelectronic Semiconductors and Efficient Devices, Department of Physics, Xiamen University, Xiamen 361005, China*

Jinrong Zhou − *Key Laboratory of Light Field Manipulation and System Integration Applications in Fujian Province, School of Physics and Information Engineering, Minnan Normal University, Zhangzhou 363000, China*

Xiuyan Li − *Key Laboratory of Light Field Manipulation and System Integration Applications in Fujian Province, School of Physics and Information Engineering, Minnan Normal University, Zhangzhou 363000, China*

Yuhong Fang − *Key Laboratory of Light Field Manipulation and System Integration Applications in Fujian Province, School of Physics and Information Engineering, Minnan Normal University, Zhangzhou 363000, China*

Complete contact information is available at: https://pubs.acs.org/10.1021/acs.energyfuels.4c03960

Notes

The authors declare no competing financial interest.

■ ACKNOWLEDGMENTS

This work was supported by the National Key Research and Development Program of China (grant no. 2022YFB3605400), the National Natural Science Foundation of China (nos. 61975072 and 12274355), Key Scientific and Technological Innovation Projects of Fujian Province (no. 2022G02006), Natural Science Foundation of Fujian Province (nos. 2022J01915, 2022J01917, and 2021J011009), the Fujian province middle and young teacher education research project (nos. JAT210276 and JAT190379), College students' innovation and entrepreneurship training program (nos. S202310402015), and teaching reform of Fujian Provincial Physics Subject Alliance (no. FJPHYS022-B11). The authors would like to thank Fonash Research Group in the Pennsylvania State University for providing the AMPS-1D simulation package. The authors thank Prof. Huanting Chen (Minnan Normal University) and Prof. Yingwen Tang (Minnan Normal University) for helpful discussion.

REFERENCES

(1) NREL. Best Research-Cell Efficiency Chart | Photovoltaic Research. https://www.nrel.gov/pv/cell-efficiency.html (accessed November 03, 2020).

(2) Zhao, Y.; Xiang, H.; Ran, R.; Zhou, W.; Wang, W.; Shao, Z. Beyond Two-dimension: One- and Zero-dimensional Halide Perovskites as New-generation Passivators for High-performance Perovskite Solar Cells. *J. Energy Chem.* **2023**, *83*, 189−208.

(3) Huang, J.; Xiang, H.; Ran, R.; Zhou, W.; Wang, W.; Shao, Z. Fundamental Understanding in the Performance-limiting Factors of $Cs_2AgBiBr_6$-based Perovskite Photovoltaics. *Renew. Sust. Energy Rev.* **2024**, *191*, 114187.

(4) Song, L. Perovskite solar cells toward industrialization: Screen printed perovskite films. *Mater. Rep.: Energy* **2022**, *2*, 100171.

(5) Wu, J.; Gao, M.; Chai, Y.; Liu, P.; Zhang, B.; Liu, J.; Ye, L. Towards A Bright Future: the Versatile Applications of Organic Solar Cells. *Mater. Rep.: Energy* **2021**, *1*, 100062.

(6) Azadinia, M.; Ameri, M.; Ghahrizjani, R. T.; Fathollahi, M. Maximizing the Performance of Single and Multijunction MA and Lead-free Perovskite Solar Cell. *Mater. Today Energy* **2021**, *20*, 100647.

(7) Lin, S.; Zhang, B.; Lü, T. Y.; Zheng, J. C.; Pan, H.; Chen, H.; Lin, C. J.; Li, X.; Zhou, J. Inorganic Lead-free B-γ-$CsSnI_3$ Perovskite Solar Cells Using Diverse Electron-Transporting Materials: A Simulation Study. *ACS Omega* **2021**, *6*, 26689−26698.

(8) Liu, D.; Li, Q.; Jing, H.; Wu, K. Pressure-induced Effects in the Inorganic Halide Perovskite $CsGeI_3$. *RSC Adv.* **2019**, *9*, 3279−3284.

(9) Raj, A.; Kumar, M.; Bherwani, H.; Gupta, A.; Anshul, A. Evidence of Improved Power Conversion Efficiency in Lead-free $CsGeI_3$ Based Perovskite Solar Cell Heterostructure via SCAPS Simulation. *J. Vac. Sci. Technol. B* **2021**, *39* (1), 012401.

(10) Chen, M.; Ju, M. G.; Garces, H. F.; Carl, A. D.; Ono, L. K.; Hawash, Z.; Zhang, Y.; Shen, T. Y.; Qi, Y.; Grimm, R. L.; Pacifici, D.; Zeng, X. C.; Zhou, Y. Y.; Padture, N. P. Highly Stable and Efficient All-inorganic Lead-free Perovskite Solar Cells with Native-oxide Passivation. *Nat. Commun.* **2019**, *10*, 16.

(11) Jong, U. G.; Yu, C. J.; Kye, Y. H.; Choe, Y. G.; Hao, W.; Li, S. First-principles Study on Structural, Electronic, and Optical Properties of Inorganic Ge-based Halide Perovskites. *Inorg. Chem.* **2019**, *58*, 4134−4140.

(12) Ju, M.-G.; Dai, J.; Ma, L.; Zeng, X. C. Lead-free Mixed Tin and Germanium Perovskites for Photovoltaic Application. *J. Am. Chem. Soc.* **2017**, *139*, 8038−8043.

(13) Li, B.; Di, H.; Chang, B.; Yin, R.; Fu, L.; Zhang, Y.; Yin, L. Efficient Passivation Strategy on Sn Related Defects for High Performance All-inorganic $CsSnI_3$ Perovskite Solar Cells. *Adv. Funct. Mater.* **2021**, *31*, 2007447.

(14) Ye, T.; Wang, X.; Wang, K.; Ma, S.; Yang, D.; Hou, Y.; Yoon, J.; Wang, K.; Priya, S. Localized Electron Density Engineering for Stabilized B-γ $CsSnI_3$-based Perovskite Solar Cells with Efficiencies > 10%. *ACS Energy Lett.* **2021**, *6*, 1480−1489.

(15) Duan, C.; Zou, F.; Wen, Q.; Qin, M.; Li, J.; Chen, C.; Lu, X.; Ding, L.; Yan, K. A Bifunctional Carbazide Additive for Durable $CsSnI_3$ Perovskite Solar Cells. *Adv. Mater.* **2023**, *35*, 2300503.

(16) Krishnamoorthy, T.; Ding, H.; Yan, C.; Leong, W. L.; Baikie, T.; Zhang, Z.; Sherburne, M.; Li, S.; Asta, M.; Mathews, N.; Mhaisalkar, S. G. Lead-free germanium iodide perovskite materials for photovoltaic applications. *J. Mater. Chem. A* **2015**, *3*, 23829−23832.

(17) Chen, L. Synthesis and Optical Properties of Lead-free Cesium Germanium Halide Perovskite Quantum Rods. *RSC Adv.* **2018**, *8*, 18396−18399.

(18) Ban, H.; Zhang, T.; Gong, X.; Sun, Q.; Zhang, X.; Pootrakulchote, N.; Shen, Y.; Wang, M. Fully Inorganic $CsSnI_3$ Mesoporous Perovskite Solar Cells with High Efficiency and Stability via Coadditive Engineering. *Sol. RRL* **2021**, *5*, 2100069.

(19) Ban, H.; Zhang, Z.; Dai, L.; Liu, Z.; Yu, H.; Shen, Y.; Zhang, X.; Zhu, J.; Wang, M. Efficient and Stable Mesoporous $CsSnI_3$ Perovskite Solar Cells via Imidazolium-based Ionic Liquid Additive. *Sol. RRL* **2022**, *6*, 2200827.

(20) Chung, I.; Lee, B.; He, J.; Chang, R. P. H.; Kanatzidis, M. G. All-solid-state Dye-sensitized Solar Cells with High Efficiency. *Nature* **2012**, *485*, 486−489.

(21) Yang, Y.-Y.; Wang, L.-S.; Xu, W.-K.; Zhang, Y.; Wang, J.-Q.; Chen, F.-X. Simulation Optimizing Planar Heterojunction Perovskite Solar Cells with $CsGeI_3$ as Hole Transport Materials. *J. Synth. Cryst.* **2017**, *46* (5), 814−819.

(22) Zheng, J. C. Asymmetrical Transport Distribution Function: Skewness as a Key to Enhance Thermoelectric Performance. *Research* **2022**, *2022*, 9867639.

(23) Jiang, M.; Tang, J. Numerical Simulation Design of All-inorganic Hole-transport-layer-free $CsSnI_3$ (Sn-rich)/$CsSnI_3$ Perovskite Efficient Solar Cells. *J. Opt. Soc. B* **2021**, *38* (12), 3754−3764.

(24) Minemoto, T.; Murata, M. Device Modeling of Perovskite Solar Cells Based on Structural Similarity with Thin Film Inorganic Semiconductor Solar Cells. *J. Appl. Phys.* **2014**, *116*, 054505.

(25) Zhu, H.; Kalkan, A. K.; Hou, J.; Fonash, S. J. Applications of AMPS-1D for solar cell simulation. *AIP Conf. Proc.* 1999, *462*, 309−314.

(26) Zheng, J. C. Universal scales of electronegativity and ionicity from electron scattering factors. *Phys. Chem. Chem. Phys.* **2024**, *26*, 19705−19723.

(27) Lambrecht, W. R. L.; Segall, B.; Andersen, O. K. Self-consistent Dipole Theory of Heterojunction Band Offsets. *Phys. Rev. B* **1990**, *41*, 2813−2831.

(28) Zheng, J. C.; Zheng, Y. M.; Wang, R. Z. Study on Valence Offsets at $In_xGa_{1-x}As/In_xAl_{1-x}As$ Heterojunction. *J. Phys.—Condens. Mater.* **1997**, *9*, 439−445.

(29) Zheng, J.-C.; Wang, R.-Z.; Zheng, Y.-M.; Cai, S.-H. Valence Offsets of Three Series of Alloy Heterojunction. *Chin. Phys. Lett.* **1997**, *14*, 775−777.

(30) Wang, H. Q.; Zheng, J. C.; Wang, R. Z.; Zheng, Y. M.; Cai, S. H. Valence-band Offsets of III-V Alloy Heterojunctions. *Surf. Interface Anal.* **1999**, *28*, 177−180.

(31) Bin, Z.; Li, J.; Wang, L.; Duan, L. Efficient n-type Dopants with Extremely Low Doping Ratios for High Performance Inverted Perovskite Solar Cells. *Energy Environ. Sci.* **2016**, *9*, 3424−3428.

(32) Nalianya, M. A.; Awino, C.; Barasa, H.; Odari, V.; Gaitho, F.; Omogo, B.; Mageto, M. Numerical Study of Lead Free $CsSn_{0.5}Ge_{0.5}I_3$ Perovskite Solar Cell by SCAPS-1D. *Optik* **2021**, *248*, 168060.

(33) Qiao, Z.; Zhang, M.; Wu, B.; Zhang, T.; Ruan, Y.; Chen, J.; Huang, L.; Wu, J.; Qi, Y.; Yang, X. Inorganic Tin-based Perovskite Solar Cells: Modeling and Performance Analysis of Hole Transport Layer-free Structures. *Chem. Phys. Lett.* **2023**, *813*, 140295.

(34) Zheng, J. C.; Zhu, Y. Searching for Higher Superconducting Transition Temperature in Strained MgB_2 Using First Principles Calculations. *Phys. Rev. B* **2006**, *73*, 024509.

(35) Li, J. J.; Dai, Y.; Zheng, J. C. Strain Engineering of Ion Migration in $LiCoO_2$. *Front. Phys.* **2022**, *17*, 13503.

(36) Zhang, W.; Du, F. Y.; Dai, Y.; Zheng, J. C. Strain Engineering of Li Ion Migration in Olivine Phosphates Cathode Materials $LiMPO_4$ (M = Mn, Fe, Co) and $(LiFePO_4)_n(LiMnPO_4)_m$ Superlattices. *Phys. Chem. Chem. Phys.* **2023**, *25*, 6142−6152.

(37) Chen, J.; Chen, F.; Xu, W.; Cao, G.; Wang, L. Simulation Optimization of Planar Heterojunction Perovskite Solar Cells with B-γ-$CsSnI_3$ as Optical Absorption Layer. *J. Synth. Cryst.* **2018**, *47* (1), 31−36.

(38) Kim, G. W.; Shinde, D. V.; Park, T. Thickness of the Hole Transport Layer in Perovskite Solar Cells: Performance versus Reproducibility. *RSC Adv.* **2015**, *5*, 99356−99360.

(39) Ouedraogo, N. A. N.; Odunmbaku, G. O.; Guo, B.; Chen, S.; Lin, X.; Shumilova, T.; Sun, K. Oxidation of spiro-OMeTAD in High-efficiency Perovskite Solar Cells. *ACS Appl. Mater. Interfaces* **2022**, *14*, 34303−34327.

(40) Alla, M.; Bimli, S.; Manjunath, V.; Samtham, M.; Kasaudhan, A.; Choudhary, E.; Rouchdi, M.; Boubker, F. Towards lead-free all-inorganic perovskite solar cell with theoretical efficiency approaching 23%. *Mater. Technol.* **2022**, *37* (14), 2963−2969.

(41) Ravidas, B. K.; Roy, M. K.; Samajdar, D. P. Investigation of Photovoltaic Performance of Lead-free $CsSnI_3$-based Perovskite Solar Cell with Different Hole Transport Layers: First Principle Calculations and SCAPS-1D Analysis. *Sol. Energy* **2023**, *249*, 163−173.

(42) Srivastava, S.; Singh, A. K.; Kumar, P.; Pradhan, B. Comparative Performance Analysis of Lead-free Perovskites Solar Cells by Numerical Simulation. *J. Appl. Phys.* **2022**, *131*, 175001.

(43) Sabbah, H. Numerical Simulation of 30% Efficient Lead-free Perovskite $CsSnGeI_3$-based Solar Cells. *Materials* **2022**, *15*, 3229.

(44) Li, X.; Li, J.; Wu, S.; Li, Y.; Peng, C.; Wu, M.; Wu, J.; Lin, J.; Ma, X.; Huang, S. Theoretical Analysis of All-inorganic Solar Cells Based on Numerical Simulation of $CsGeI_3/CsPbI_3$ with p-p+ Built-in Electric Field. *Sol. Energy* **2022**, *247*, 315−329.

(45) Le Corre, V. M.; Stolterfoht, M.; Perdigón Toro, L.; Feuerstein, M.; Wolff, C.; Gil-Escrig, L.; Bolink, H. J.; Neher, D.; Koster, L. J. A. Charge transport layers limiting the efficiency of perovskite solar cells: how to optimize conductivity, doping, and thickness. *ACS Appl. Energy Mater.* **2019**, *2*, 6280−6287.

(46) Hu, J.; Gouda, L.; Kama, A.; Tirosh, S.; Gottesman, R. Radiative recombination changes under light-soaking in $CsPbBr_3$ films on TiO_2 and insulating glass contacts: interface versus bulk effects. *ACS Appl. Energy Mater.* **2019**, *2*, 3013−3016.